On numerical broadening of particle-size spectra: a condensational growth study using PyMPDATA 1.0

Michael Olesik[1], **Jakub Banaśkiewicz**[1], **Piotr Bartman**[1], **Manuel Baumgartner**[2,3], **Simon Unterstrasser**[4], and **Sylwester Arabas**[5,1]

[1]Jagiellonian University, Kraków, Poland
[2]Zentrum für Datenverarbeitung, Johannes Gutenberg University Mainz, Germany
[3]Institute for Atmospheric Physics, Johannes Gutenberg University Mainz, Germany
[4]German Aerospace Center (DLR), Oberpfaffenhofen, Germany
[5]University of Illinois at Urbana-Champaign, Urbana, IL, USA

Correspondence: Michael Olesik (michael.olesik@doctoral.uj.edu.pl)

Abstract. This work discusses the numerical aspects of representing the diffusional (condensational) growth in particulate systems such as atmospheric clouds. It focuses on the Eulerian modelling approach, in which the evolution of the probability density function describing the particle-size spectrum is carried out using a fixed-bin discretisation (so-called "bin" microphysics). The numerical diffusion problem inherent to the employment of the fixed-bin discretisation in the numerical solution of the arising transport problem is scrutinised. The focus is on the applications of the Multidimensional Positive Definite Advection Transport Algorithm (MPDATA). Several MPDATA variants are explored including infinite-gauge, non-oscillatory, third-order-terms and recursive antidiffusive correction (Double-Pass Donor-Cell, DPDC) options. Methodology for handling coordinate transformations associated with both particle-size spectrum variable choice and numerical grid layout are expounded. The study uses PyMPDATA - a new open-source Python implementation of MPDATA. Analysis of the performance of the scheme for different discretisation parameters and different settings of the algorithm is performed using: (i) an analytically solvable box-model test case, and (ii) the single-column kinematic driver ("KiD") test case in which the size-spectral advection due to condensation is solved simultaneously with the spatial advection in the vertical physical coordinate, and in which the supersaturation evolution is coupled with the droplet growth through water mass budget. The single-column problem involves a numerical solution of a two-dimensional advection problem (spectral and spatial dimensions). The discussion presented in the paper covers size-spectral, spatial and temporal convergence, computational cost, conservativeness and quantification of the numerical broadening of the particle-size spectrum. The box-model simulations demonstrate that, for the problem considered, even a tenfold decrease of the spurious numerical spectral broadening can be obtained by an apt choice of the MPDATA variant (maintaining the same spatial and temporal resolution), yet at an increased computational cost. Analyses using the single-column test case reveal that the width of the droplet size spectrum is affected by numerical diffusion pertinent to both spatial and spectral advection. Application of even a single corrective iteration of MPDATA robustly decreases the relative dispersion of the droplet spectrum, roughly by a factor of two at the levels of maximal liquid water content.

1 Introduction

1.1 Motivation and outline

The focus of this paper is on the problem of particle-size evolution for a population of droplets undergoing diffusional growth. Representing the particle-size spectrum using a number density function, the problem can be stated using a population-balance equation expressing conservation of the number of particles. Herein, the numerical solution of the problem using the MPDATA family of finite difference schemes originating in Smolarkiewicz (1983, 1984) is discussed. MPDATA stands for Multidimensional Positive Definite Advection Transport Algorithm and is a higher-order iterative extension of the forward-in-time upwind scheme.

MPDATA features a variety of options allowing to pick an algorithm variant appropriate to the problem at hand. This work highlights the importance of the MPDATA algorithm variant choice for the resultant spectral broadening of the particle-size spectrum. The term spectral broadening refers to the increasing width of the droplet spectrum during the lifetime of a cloud, which may be associated with both physical mechanisms (mixing, turbulence) as well as spurious artefacts stemming from the employed numerical solution technique.

Cloud simulations with a detailed treatment of droplet microphysics face a twofold challenge in resolving the droplet spectrum width. First, it is challenging to model and numerically represent the subtleties of condensational growth (e.g., Arabas and Shima, 2017; Yang et al., 2018), even more so when considering the interplay between particle population dynamics and supersaturation fluctuations (e.g., Jeffery et al., 2007; Abade et al., 2018). Second, the discretisation strategies employed in representing the particle-size spectrum and its evolution are characterised by inherent limitations which constrain the fidelity of spectral width predictions (e.g., Arabas and Pawlowska, 2011; Morrison et al., 2018). Finally, corroboration of spectral width estimates from both theory and modelling against experimental data faces the problems of instrumental broadening inherent to the measurement techniques (e.g. Devenish et al., 2012, sec. 3.2) and the problem of sampling volume choice (e.g., Kostinski and Jameson, 2000).

The width of the spectrum plays a key role in the determination of both the droplet collision probabilities (Grabowski and Wang, 2013) and the characteristics relevant for radiative transfer (Chandrakar et al., 2018). These in turn are reflected in parameterisations of cloud processes in large-scale models. Taking climate-timescale simulation as an example, the representation of clouds remains the largest source of uncertainty (Schneider et al., 2017). The parameterisations used in climate models are developed based on smaller-scale simulations resolving particle-size spectrum evolution. Consequently, it is of high interest to quantify the extent to which the droplet-size spectrum width is a consequence of (a) the physics of particle growth embodied in the governing equations and (b) the discretisation and the associated numerical diffusion.

The following introductory subsections start with a literature review of applications of MPDATA to the problem of condensational growth of particles. Section 2 focuses on a simple box-model test case and serves as a tutorial on MPDATA variants (limited to one-dimensional homogeneous advection of a positive-sign signal). It is presented to gather the information that is scattered across works focusing on more complex computational fluid dynamics applications of MPDATA. Example simulations employing an analytically solvable test case pertaining to the evolution of cloud droplet size spectrum in a cumulus cloud is used to depict the effects on numerical broadening from enabling the discussed algorithm variants. An analysis of the computational cost of different algorithm variants is carried out and corroborated with previously published data. While comprehensive from the point of view of the considered problem of diffusional growth, the presented material merely hints at the versatility of the algorithm. For a proper review of the MPDATA family of algorithms highlighting the multi-dimensional aspects and its multifaceted applications, we refer to Smolarkiewicz and Margolin (1998), Smolarkiewicz (2006) and Kühnlein and Smolarkiewicz (2017).

Section 3 covers the application of MPDATA for coupled size-spectral and spatial advection in a single-column kinematic setup from Shipway and Hill (2012). First, the methodology to handle the spectral-spatial liquid water advection problem taking into account the coupling with the vapour field is detailed. Second, the results obtained using different MPDATA variants are discussed focusing on the measures of spectral broadening. title = PyMPDATA v1: Numba-accelerated implementation of1MPDATA with examples in Python, Julia and Matlab,

Section 4 concludes the work with a summary of findings. Appendix A contains convergence analysis based on results of multiple simulations using the embraced box-model test case run with different temporal and spatial (size-spectral) resolutions.

All presented simulations are performed with the open-source package PyMPDATA Bartman et al. (2021).

1.2 Background

There exist two contrasting approaches for modelling the evolution of droplet-size spectrum (see Grabowski, 2020, for a review): Eulerian (fixed-bin) and the Lagrangian (moving-bin, moving-sectional or particle-based). Overall, while the Lagrangian methods are the focus of active research and development (Morrison et al., 2020), the Eulerian schemes have been predominantly used in large-scale modelling (Khain et al., 2015).

Following Liu et al. (1997) and Morrison et al. (2018), the earliest documented study employing the Eulerian numerics for condensational growth of a population of particles is that of Kovetz and Olund (1969). Several earlier works, starting with the seminal study of Howell (1949), utilised the Lagrangian approach. The numerical scheme proposed in Kovetz and Olund (1969, eq. (10)) resembles an upwind algorithm being explicit in time and orienting the finite-difference stencil differently for condensation and evaporation.

One of the first discussions of numerical broadening of the spectrum can likely be found in Brown (1980) where the numerical scheme from Kovetz and Olund (1969) was improved in several ways, including the sampling of the drop growth rate at the bin boundaries (as is done herein). Brown

(1980) also covers quantification of the error of the method by comparisons to analytic solutions.

In Tsang and Brock (1982), the authors point out that upwind differencing is not suitable for aerosol growth calculations due to its unacceptable numerical diffusion. Noteworthy, the study includes considerations of the Kelvin effect of surface tension on the drop growth (not considered herein, see discussion of eq. 2.3 below).

The first mention of an application of the MPDATA scheme for the problem of condensational growth can be found in Smolarkiewicz (1984). The problem is given as an example where the divergent-flow option of the algorithm may be applicable (see sect. 2.8 below).

In Tsang and Korgaonkar (1987), which is focused on evaporation, MPDATA is used as a predictor step followed by a corrective step using a Galerkin finite element solver. In two subsequent studies from the same group (Tsang and Rao, 1988, 1990), MPDATA is compared to other algorithms in terms of conservativeness and computational cost. In Tsang and Rao (1988), the basic 3-iteration MPDATA was used. Interestingly, it is noted there that "*If the antidiffusion velocities are increased by some factor between 1.04 and 1.08, use of [corrective iteration] only once can reduce 50% of the computing time [...] without much sacrifice of accuracy*". In conclusion, the authors praise MPDATA for providing narrow size spectra. Tsang and Rao (1988) pointed out that MPDATA performs worse than the upwind scheme in terms of the prediction accuracy of the mean radius.

The "Aerosol Science: Theory and Practice" book of Williams and Loyalka (1991) contains a section (5.19) on MPDATA (termed "Smolarkiewicz method") within a chapter focusing on the methods of solving the dynamic equation describing aerosol spectrum evolution. The basic variant of MPDATA (Smolarkiewicz, 1983) was presented with an outline of its derivation.

In Kostoglou and Karabelas (1995) and Dhaniyala and Wexler (1996), the authors mention that MPDATA has the potential to reduce the numerical diffusion as compared to upwind in the context of particle size evolution calculations. The first lists high computational cost among drawbacks in using the algorithm that led to discarding the scheme from the presented comparison.

In Morrison et al. (2018), a comparison of different numerical schemes for the condensational growth problem is performed. Both fixed-, and moving-bin approaches are compared, including the non-oscillatory variant of MPDATA (referred to as MPDG therein). MPDATA is reported to produce more significant numerical diffusion and spectral broadening than all other methods. Intriguingly, as can be seen in Fig. 7 therein, the broad spectrum in the results obtained with MPDATA appears already at the very beginning of the simulations, at the altitude of 20m out of 520m of simulated displacement of an air parcel.

In Wei et al. (2020), MPDATA is employed for integrating droplet spectrum evolution for comparison with a Lagrangian scheme. The work concludes that the spurious broadening of the spectrum cannot be alleviated even with a grid composed of 2000 size bins.

The discussion presented in Morrison et al. (2018) prompted further analyses presented in Hernandéz Pardo et al. (2020) and Lee et al. (2021). These studies highlighted that, in principle, the problem is a four-dimensional transport problem (three spatial dimensions and the spectral dimension) and that the interplay of spectral and spatial advection further nuances the issue of spectral broadening.

Noteworthy, none of the works mentioned above discussed coordinate transformations to non-linear grid layouts with MPDATA (a discussion of handling non-uniform mesh with the upwind scheme can be found in Li et al., 2017, Appendix A). Wei et al. (2020) and Morrison et al. (2018) are the only works mentioning other than the basic flavour of the scheme, yet only the non-oscillatory option was considered. Herein, the applicability for solving the condensational growth problem of multiple variants of MPDATA and their combinations is expounded.

1.3 Governing equations

To describe the conservation of particle number N under the evolution of the particle-size spectrum $n_p(p) = \frac{dN}{dp}$ (n denoting number density as a function of particle-size parameter p such as radius or volume), one may take the one-dimensional continuity equation (i.e., Liouville equation expressing the conservation of probability, for discussion see Hulburt and Katz, 1964), in a generalised coordinate system:

$$\partial_t(Gn_p) + \partial_x(uGn_p) = 0, \tag{1.1}$$

where $G \equiv G(x)$ represents the coordinate transformation from p to x with x being an equidistant mesh coordinate used in the numerical solution; $n_p \equiv n_p(p(x))$ being number density function and $u \equiv u(x)$ denoting the pace of particle growth in the chosen coordinate x. The coordinate transformation term G may play a twofold role in this context.

First, there is a degree of freedom in the choice of the particle-size parameter used as the coordinate (i.e., the argument p of the density function $n(p)$). For the chosen coordinates $p \in [r, s \sim r^2, v \sim r^3]$, the appropriate distributions will be $n_r(r)$, $n_s(s)$ and $n_v(v)$ where $s = 4\pi r^2$ and $v = 4/3\pi r^3$ denote particle surface and volume, respectively. The size spectrum $n_p(p)$ in a given coordinate is related with $n_r(r)$ via the following relation of measures: $n_p(p)dp = n_r(r)dr$ so the total number $N = \int n_r dr$ is conserved.

Second, there is also a degree of freedom in the choice of the grid layout $p(r(x))$, that is how the parameters r, s or v are discretised to form the equidistant grid in x. This can be used, for instance, to define a mass-doubling grid layout ($x = \ln_2(r^3)$) as used in Morrison et al. (2018) and herein.

Combining the two transformations results in the following definition of G:

$$G \equiv dp(r)/dx(r) = \frac{dp}{dx} \tag{1.2}$$

which defines the transformation from the coordinate p of the density function to the numerical mesh coordinate x. For further discussion of the coordinate transformation approaches in the embraced framework (including multi-dimensional setting), see Smolarkiewicz and Clark (1986) and Smolarkiewicz and Margolin (1993).

2 Spectral advection with upwind and MPDATA (box-model test case)

2.1 Upwind discretisation

The numerical solution of equation (1.1) is obtained on a grid defined by $x = \mathrm{i} \cdot \Delta x$ and at discrete timesteps defined by $t = \mathrm{n} \cdot \Delta t$. Henceforth, $\psi_\mathrm{i}^\mathrm{n}$ and G_i denote the discretised number density n_p and the discretised coordinate transformation term, respectively. The dimensionless advective field is denoted by $GC = \frac{dp}{dx} u \Delta t / \Delta x$, where C stands for the Courant number, i.e. the velocity in terms of temporal and spatial grid increments. Note that the values of the Courant number itself are not used, only the product GC of the coordinate transformation term G and the Courant number C. A staggered grid is employed and indicated with fractional indices for vector fields, e.g.,: $GC_{\mathrm{i}+1/2} \equiv (GC)|_{\mathrm{i}+1/2}$ in the case of the discretisation of GC. A finite difference form of the differential operators is introduced embracing the so-called upwind approach (dating back at least to Courant et al., 1952, eq. 16 therein):

$$\begin{aligned}\psi_\mathrm{i}^{\mathrm{n}+1} = \psi_\mathrm{i}^\mathrm{n} - \frac{1}{G_\mathrm{i}} \big(& F(\psi_\mathrm{i}^\mathrm{n}, \psi_{\mathrm{i}+1}^{n}, GC_{\mathrm{i}+1/2}) - \\ & F(\psi_{\mathrm{i}-1}^\mathrm{n}, \psi_\mathrm{i}^\mathrm{n}, GC_{\mathrm{i}-1/2}) \big)\end{aligned} \tag{2.1}$$

with

$$\begin{aligned}F(\psi_L, \psi_R, GC_\mathrm{mid}) = & \max(GC_\mathrm{mid}, 0) \cdot \psi_L + \\ & \min(GC_\mathrm{mid}, 0) \cdot \psi_R\end{aligned} \tag{2.2}$$

where the introduced flux function F defines the flux of ψ across a grid-cell boundary. Hereinafter a shorthand notation $F_{i+\frac{1}{2}}(\psi) \equiv F(\psi_i, \psi_{i+1}, GC_{i+\frac{1}{2}})$ is used.

2.2 Box-model test case and upwind solution

The test case is based on Figure 3 from East (1957) - one of the early papers on the topic of cloud droplet spectral broadening. The case considers the growth of a population of cloud droplets through condensation in the equilibrium supersaturation limit, where:

$$u \approx \frac{dx}{dr} \dot{r} = \frac{dx}{dr} \frac{\xi}{r}, \tag{2.3}$$

with $\xi = \xi_0 (S-1)$ being an approximately constant factor proportional to the supersaturation $(S-1)$ where the saturation S is equal to the relative humidity of ambient air. The parameter ξ_0 is set to $100\ \mathrm{\mu m^2 s^{-1}}$ to match the results from East (1957). The approximation (2.3) neglects the dependence of particle growth rate on the surface tension (Kelvin term). Taking it into consideration requires replacing $(S-1)$ with $(S - e^{A/r})$, where A depends on temperature only; for discussion see, e.g., Tsang and Brock (1982).

For the initial number density function, an idealised fair-weather cumulus droplet size spectrum is modelled with a lognormal distribution:

$$n_r^{(0)}(r) = n_0 \exp\left(-\kappa (\log_{10}(r/r_0))^2\right)/r \tag{2.4}$$

with $r_0 = 7\ \mathrm{\mu m}$ and $\kappa = 22$ (East and Marshall, 1954) while was set at $n_0 = 465\ \mathrm{cm^{-3}}$ to match liquid water content of $1\ \mathrm{g\,kg^{-1}}$ as indicated in East (1957).

For the boundary conditions (implemented using halo grid cells), extrapolation is applied for G, while both ψ and GC are set to zero within the halo.

Analytical solution to eq. (1.1) is readily obtainable for $\dot{r} = \xi / r$ and for any initial size spectrum. Noting that introducing $x = r^2$ coordinates, the transport equation (1.1) becomes a constant-coefficient advection equation, the problem reduces to translation of the signal in x by $2\xi t$. Cast in the r coordinate, the solution can be expressed as (Kovetz, 1969):

$$\psi^\text{analytical} = n_r(r, t > 0) \equiv \frac{r}{\tilde{r}} n_r^{(0)}(\tilde{r}), \tag{2.5}$$

where $\tilde{r} = \tilde{r}(r,t) = \sqrt{r^2 - 2\xi t}$.

The upper panels in Figures 1 and 2 depict the droplet size spectrum evolution through condensational growth from an initial liquid water mixing ratio of $M_0 = 1\ \mathrm{g\,kg^{-1}}$ under supersaturation $S - 1 = 0.075\%$.

Two grid layout (x) and size parameter (p) choices are depicted. Both panels in Fig. 1 present simulation carried out with $p = r^2$ coordinate and discretised on a mass-doubling grid ($x = \ln_2(r^3)$). Both panels in Fig. 2 present simulation results obtained with $x = r$ and $p = r$. In all cases, the timestep is set to $\Delta t = \frac{1}{3}$ s. The domain span is 1–26 µm. The grid is composed of 75 grid cells. Such settings corresponds to $GC \approx 0.26$ for $p = r^2$, and a variable Courant number approximately in the range of 0.03 to 0.07 for $p = r$.

The time steps depicted in the plots are selected by finding t for which the integrated liquid water mixing ratio of the analytical solution equals to 1, 4 and $10\ \mathrm{g\,kg^{-1}}$ (assuming air density of $1\ \mathrm{kg\,m^{-3}}$). In both Figure 1 and 2, the upper panels display the number density and the bottom panels show the normalised mass density. The bottom panels thus depict the same quantities as Fig. 3 in East (1957).

The normalised mass density of bin i is evaluated as $4/3\pi\rho_l m_i^{(l=3)}/M$ by calculating the third statistical moment

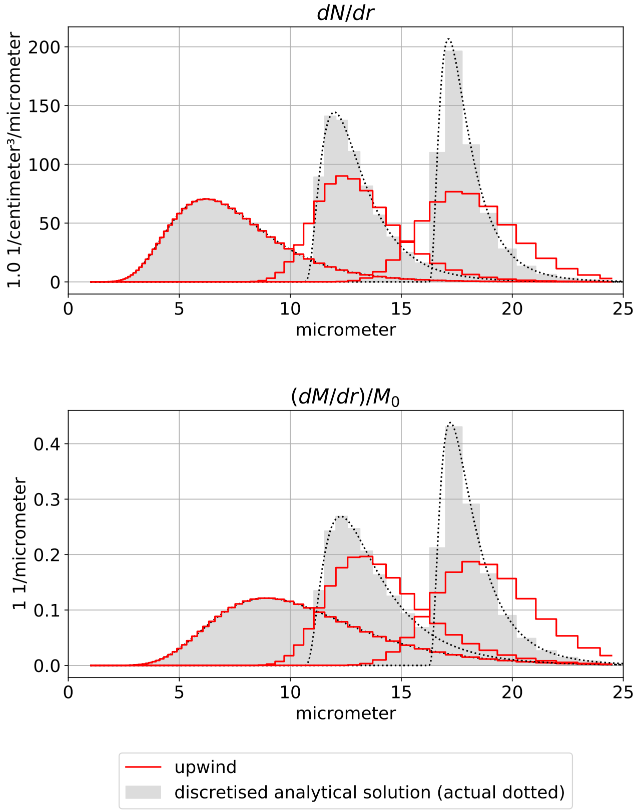

Figure 1. Evolution of the particle number density (upper panel) and normalised mass density (bottom panel) with red histograms corresponding to the numerical solution using upwind scheme, black dots depicting analytical solution, and grey filled histogram representing discretised analytical solution; compare Fig. 3 in East (1957). Numerical solution was obtained in the following coordinate transformation: $p = r^2$; $x = \ln_2(r^3)$

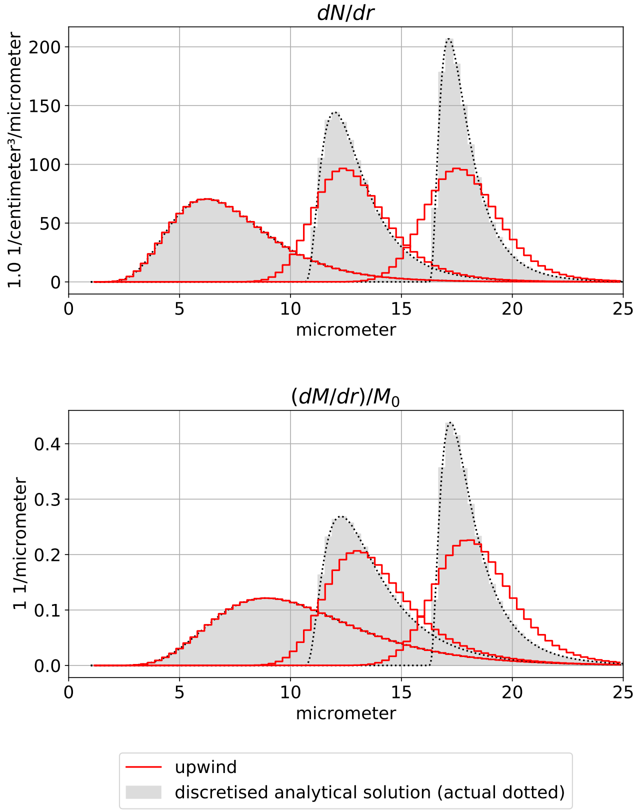

Figure 2. As in Fig. 1 for $p = r$ and $x = r$.

of the number distribution $n_r(p)$ with the formula:

$$m_i^{(l)} = \int_{r_1}^{r_2} n_r r^l dr = \tag{2.6}$$

$$= \psi_i \cdot \begin{cases} (l+1)^{-1} r^{l+1} \Big|_{r_1}^{r_2} & \text{for } \; p = r \\ 2\,(l+2)^{-1} \left(r^2\right)^{\frac{l+2}{2}} \Big|_{r_1^2}^{r_2^2} & \text{for } \; p = r^2 \end{cases}$$

where r_1, r_2 are the boundaries of i-th bin, and ψ_i is the value of n_p associated with the bin (i.e., n_p is assumed to be bin-wise constant; note that the dimension of n_p depends on the choice of p). The normalisation factor M is the mixing ratio (e.g., $M = M_0 = 1\ \mathrm{g\,kg^{-1}}$ for $t = 0$).

The dotted curve corresponds to the analytic solution. The numerical solution obtained with the upwind scheme (2.1) is plotted with red histograms and compared to the discretised analytical solution plotted as grey filled histograms.

Looking at the mass density plots in Figs. 1 and 2, it is evident that casting the results in the form of mass density shifts positions of the extrema in comparison with the analytical solution. This is one of the consequences of integrating the number conservation law (for discussion see sec. 2.12).

As can be seen in both the number- and mass-density plots in Figs. 1 and 2, solutions obtained with the upwind scheme are characterised by a significant drop in the peak value and spectral broadening with respect to the analytical solution – both manifesting the numerical diffusion.

The broadening and the drop in the peak value are less pronounced in Fig. 2 where the linear grid increases the resolution in the large-particle region of the spectrum.

2.3 Truncation error analysis of the upwind scheme

One of the methods used to quantify the numerical diffusion of the upwind scheme is the modified equation analysis of Hirt (1968) (see Margolin and Shashkov, 2006, for discussion in the context of MPDATA). To depict the idea, a simplified setting of $G = 1$ and $C = \text{const}$ is outlined herein. In the analysis, the Taylor expansion of ψ up to the second order is taken at ψ_i^{n+1}, ψ_{i+1}^{n} and ψ_{i-1}^{n} and substituted into the numerical upwind scheme, in which the flux function (2.2) is expressed using moduli (e.g., Crowley, 1968, eq. (12)):

$$\psi_i^{n+1} = \psi_i^n - \left(\frac{C+|C|}{2}(\psi_i^n - \psi_{i-1}^n) + \frac{C-|C|}{2}(\psi_{i+1}^n - \psi_i^n)\right) \tag{2.7}$$

resulting in:

$$\partial_t\psi + \partial_t^2\psi\frac{\Delta t}{2} = -\frac{u+|u|}{2}\left(\partial_x\psi - \partial_x^2\psi\frac{\Delta x}{2}\right) - \frac{u-|u|}{2}\left(\partial_x\psi + \partial_x^2\psi\frac{\Delta x}{2}\right) \tag{2.8}$$

which is further transformed by employing a time derivative of both sides of the original advection equation $\partial_t\psi = -u\partial_x\psi \longrightarrow \partial_t^2\psi = -u\partial_x\partial_t\psi = u^2\partial_x^2\psi$ to substitute the second-order time derivative with spatial derivative (Cauchy-Kowalevski procedure, see Toro, 1999) leading to the sought modified equation (Roberts and Weiss, 1966, eq. 2.9):

$$\partial_t\psi + u\partial_x\psi + \underbrace{\left(u^2\frac{\Delta t}{2} - |u|\frac{\Delta x}{2}\right)}_{\mathrm{K}}\partial_x^2\psi + ... = 0 \tag{2.9}$$

The above analysis depicts that the employment of the numerical scheme (2.1) results in a solution of a modified equation (2.9), approximating the original problem up to first order. The leading second-order error contribution has the form of a diffusive term with a coefficient K (note that the above outline of the modified equation analysis assumes the constant velocity field). The diffusive form of the leading error term explains with the smoothing of the spectrum evident in Figs. 1,2, and hence the notion of numerical diffusion.

2.4 Antidiffusive velocity and iterative corrections

The problem of numerical diffusion can be addressed by introducing the so-called “antidiffusive velocity" (Smolarkiewicz, 1983). To this end, the Fickian flux can be cast in the form of the advective flux - an approach dubbed pseudo-velocity technique in the context of advection-diffusion simulations (Lange, 1973, 1978) or hyperbolic formulation of diffusion (Cristiani, 2015, discussion of eq. (4) therein), and discussed in detail in Smolarkiewicz and Clark (1986, sect. 3.2):

$$\partial_x(K\partial_x\psi) = \partial_x\left(K\frac{\partial_x\psi}{\psi}\psi\right). \tag{2.10}$$

In Smolarkiewicz (1983, 1984), it was proposed to apply the identity (2.10) to equation (2.9) to suppress the spurious diffusion. The procedure is iterative. The first iteration is the basic upwind pass. Subsequent corrective iterations reverse the effect of numerical diffusion by performing upwind passes with the so-called antidiffusive flux based on equation (2.10) but with K taken with a negative sign and approximated using the upwind stencil (for discussion of the discretisation, see Smolarkiewicz and Margolin (2001)).

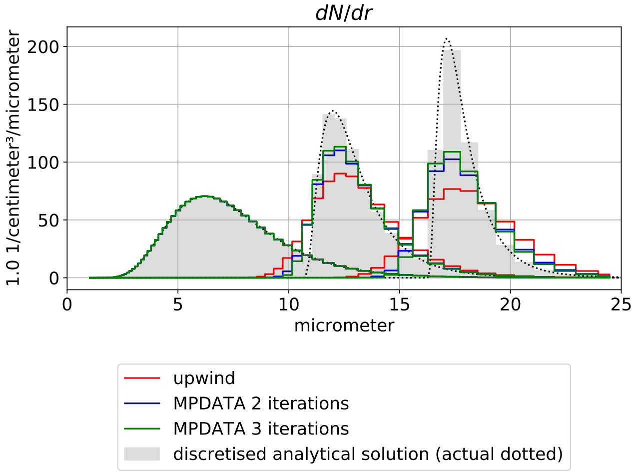

Figure 3. Comparison of analytic, upwind and MPDATA solutions (see plot key for algorithm variant specification) using the setup from Fig. 1, see sec. 2.4 for discussion.

Accordingly, the basic antidiffusive field $GC^{(k)}$ is defined as follows (with $\epsilon > 0$ being an arbitrarily small constant used to prevent from divisions by zero):

$$GC^{(k)}_{i+\frac{1}{2}} = A_{i+\frac{1}{2}}\left(\left|GC^{(k-1)}_{i+\frac{1}{2}}\right| - \left(GC^{(k-1)}_{i+\frac{1}{2}}\right)^2\right), \tag{2.11}$$

where k is the iteration number, $GC^{(1)} \equiv GC$ and

$$A_{i+\frac{1}{2}} = \frac{\psi^*_{i+1} - \psi^*_i}{\psi^*_{i+1} + \psi^*_i + \epsilon}, \tag{2.12}$$

where ψ^* denotes ψ^n in the first iteration, or the values resulting from the application of the upwind scheme with the antidiffusive flux in subsequent iterations. The MPDATA scheme inherits the key properties of upwind in terms of positive-definiteness, conservativeness and stability while reducing the effect of numerical diffusion. Given the context of conservation of particle concentration, in all presented numerical formulæ below, it is assumed that the transported signal is positive, the references provided include formulation of the algorithm for variable sign signals.

Figure 3 compares a set of example simulations performed with the same set-up as in Figure 1. The analytical results obtained with upwind are supplemented with results obtained using the MPDATA scheme with two and three iterations. Employment of the MPDATA iteration corrects both the signal peak amplitude and its width, as well as the position of the maximum. It is visible that the effect of the third iteration is less pronounced than that of the second one. Overall, while the MPDATA solutions are superior to upwind, the drop in amplitude and broadening of the resultant spectrum still visibly differs from the discretised analytical solution.

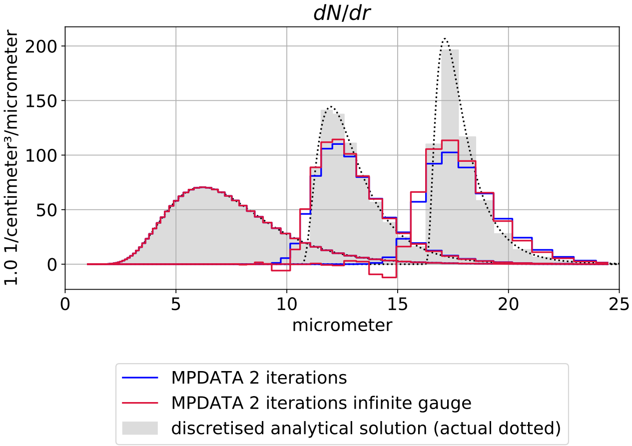

Figure 4. Comparison of analytic, upwind and MPDATA solutions (see plot key for algorithm variant specification) using the setup from Fig. 1, see sec. 2.5 for discussion.

2.5 Infinite gauge variant

For the possible improvement of the algorithm, one may consider linearising MPDATA about an arbitrarily large constant (i.e. taking $\psi' = \psi + a\chi$ in the limit $a \longrightarrow \infty$ instead of ψ, where χ is a constant scalar background field). Such analysis was considered in Smolarkiewicz and Clark (1986, eq. 41) and subsequently referred to as the "infinite-gauge" (or "iga") variant of MPDATA (Smolarkiewicz (2006, eq. 34), Margolin and Shashkov (2006, point (6) on page 1204)).

Such gauge transformation changes the corrective iterations of the basic algorithm as follows (replacing eqs. (2.12) and (2.2) what is symbolised with $\rightsquigarrow$):

$$A_{i+\frac{1}{2}} \quad \rightsquigarrow \quad A^{(\text{iga})}_{i+\frac{1}{2}} = \frac{\psi^*_{i+1} - \psi^*_i}{2} \tag{2.13}$$

$$F_{i+\frac{1}{2}} \quad \rightsquigarrow \quad F^{(\text{iga})}_{i+\frac{1}{2}} = GC^{(k)}_{i+\frac{1}{2}} \tag{2.14}$$

Noting that the amplitude of the diffusive flux (2.10) is inversely proportional to the amplitude of the signal, such gauge choice decreases the amplitude of the truncation error (see Smolarkiewicz and Clark (1986, p. 408), Jaruga et al. (2015, discussion of Fig. 11)), however, it makes the algorithm no longer positive definite.

Figure 4 depicts how enabling the infinite gauge variant influences results presented in Figure 3. In each plotted timestep, the maximum amplitude of the infinite-gauge result is closest to the analytical solution improving over the basic MPDATA. However, in each case, negative values are observed (non-physical in case of the considered problem).

Consequently, for the problem at hand, it is effectively essential to combine it with the monotonicity-preserving non-oscillatory option outlined in the next section.

2.6 Non-oscillatory option

In Smolarkiewicz and Grabowski (1990), an extension of the MPDATA algorithm was introduced that makes the solution monotonicity preserving and precludes the appearance of negative values in the discussed solution of droplet size spectrum evolution. The trade-off is that the order of the algorithm is reduced (see Appendix A).

The non-oscillatory option (later referred to as "non-osc" herein) modifies the algorithm in such way:

$$GC^{(k+1)}_{i+\frac{1}{2}} \rightsquigarrow GC^{(k+1,\text{non-osc})}_{i+\frac{1}{2}} = GC^{(k)}_{i+\frac{1}{2}} \times \\ \times \begin{cases} \min(1,\beta^{\downarrow}_i,\beta^{\uparrow}_{i+1}) & GC^{(k)}_{i+\frac{1}{2}} \geq 0 \\ \min(1,\beta^{\uparrow}_i,\beta^{\downarrow}_{i+1}) & GC^{(k)}_{i+\frac{1}{2}} < 0 \end{cases}, \tag{2.15}$$

where

$$\beta^{\uparrow}_i \equiv G_i \times \frac{\max\left(\psi^{(\max)}_i, \psi^*_{i-1}, \psi^*_i, \psi^*_{i+1}\right) - \psi^*_i}{\max\left(F(\psi^*)_{i-\frac{1}{2}}, 0\right) - \min\left(F(\psi^*_i)_{i+\frac{1}{2}}, 0\right) + \epsilon}, \tag{2.16}$$

and

$$\beta^{\downarrow}_i \equiv G_i \times \frac{\min\left(\psi^{(\min)}_i, \psi^*_{i-1}, \psi^*_i, \psi^*_{i+1}\right) - \psi^*_i}{\max\left(F(\psi^*_i)_{i+\frac{1}{2}}, 0\right) - \min\left(F(\psi^*_i)_{i-\frac{1}{2}}, 0\right) + \epsilon}, \tag{2.17}$$

with

$$\psi^{(\min)}_i = \min(\psi^n_{i-1}, \psi^n_i, \psi^n_{i+1}), \tag{2.18}$$

$$\psi^{(\max)}_i = \max(\psi^n_{i-1}, \psi^n_i, \psi^n_{i+1}). \tag{2.19}$$

Note that in the case of infinite gauge option enabled, F function takes form presented in eq. (2.13) (see also Hill, 2011, sect. 2.5).

Figure 5 juxtaposes infinite gauge solutions with the non-oscillatory option switched on or off. The effectiveness of the latter variant is apparent as spurious negative values no longer occur.

2.7 DPDC

An alternative approach to the iterative procedure was introduced in Beason and Margolin (1988); Margolin and Smolarkiewicz (1998) and further discussed in Margolin and Shashkov (2006), where the contributions of multiple corrective iterations of MPDATA were analytically summed leading to a new two-pass scheme dubbed DPDC (Double-Pass Donor-Cell), featuring the following form of the antidiffusive GC field:

$$GC^{(2)}_{i+\frac{1}{2}} \rightsquigarrow GC^{(\text{DPDC})}_{i+\frac{1}{2}} = \frac{GC^{(2)}}{1 - |A_{i+\frac{1}{2}}|}\left(1 - \frac{GC^{(2)}}{1 - A^2_{i+\frac{1}{2}}}\right), \tag{2.20}$$

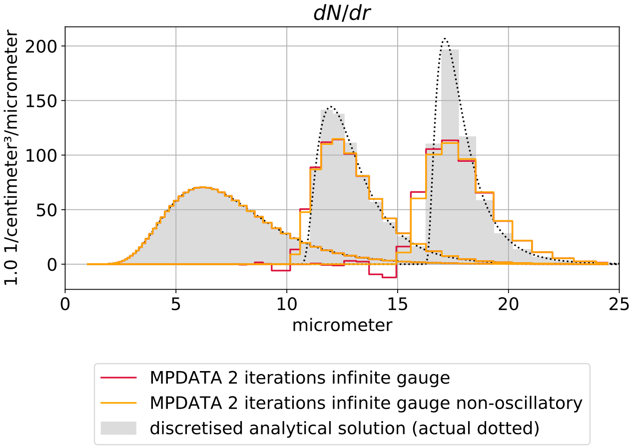

Figure 5. Comparison of analytic, upwind and MPDATA solutions (see plot key for algorithm variant specification) using the setup from Fig. 1, see sec. 2.6 for discussion.

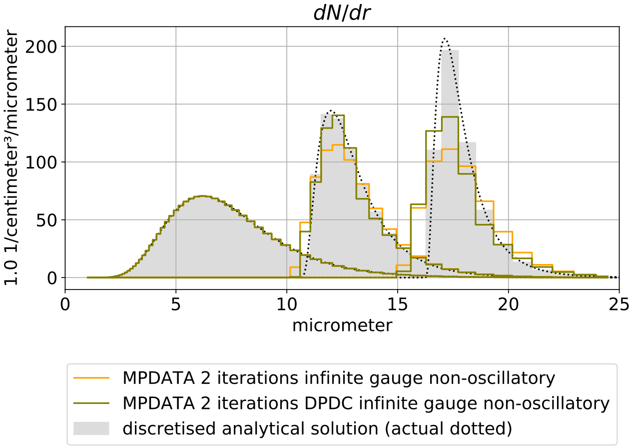

Figure 6. Comparison of analytic, upwind and MPDATA solutions (see plot key for algorithm variant specification) using the setup from Fig. 1, see sec. 2.7 for discussion.

with $A_{i+\frac{1}{2}}$ defined in eq. (2.12). Note that only one corrective iteration is performed with the DPDC variant.

As in the case of the infinite gauge variant of MPDATA (section 2.5), the above formulation does not guarantee the monotonicity of the solution. Herein an example simulation combining the double-pass (DPDC), the non-oscillatory and infinite-gauge variants is presented in Figure 6 depicting how the solution is improved over that in Figure 5.

2.8 Divergent-flow correction

For divergent flow (hereinafter abbreviated dfl), modified equation analysis yields an additional correction term to the antidiffusive velocity (see Smolarkiewicz (1984, eq. (38)) for uniform coordinates, Margolin and Smolarkiewicz (1998, eq. (30)) for non-uniform coordinates and Waruszewski et al. (2018, sect. 4) for the infinite-gauge variant):

$$
\begin{aligned}
GC^{(k)}_{i+\frac{1}{2}} \rightsquigarrow GC^{(\text{k,dfl})}_{i+\frac{1}{2}} = GC^{(k)} &- \frac{GC^{(k)}_{i+\frac{1}{2}}}{G_{i+1}+G_i} \times \\
&\times \frac{GC^{(k)}_{i+\frac{3}{2}} - GC^{(k)}_{i-1/2}}{2} \times \\
&\times \begin{cases} (\psi^*_{i+1}+\psi^*_i)/2 & (iga) \\ 1 & (else) \end{cases}
\end{aligned} \qquad (2.21)
$$

As pointed out in section 5.1 in Smolarkiewicz (1984), this option has the potential of improving results for the problem of the evolution of the droplet size spectrum (personal communication with William Hall cited therein). This is due to the drop growth velocity defined by eq. (2.3) being dependent on the droplet radius (hence divergent given the one-dimensional problem). Yet, applying adequate coordinate transformation (i.e., $p = r^2$), the drop growth velocity in the transformed coordinates becomes constant (see section 2.2 above and Hall (see, e.g. 1980, sec. 3b)). However, in simulations using the presented setup (for $p \neq r^2$; not shown), only insignificant changes in the signal occurring when the divergent-flow option was used were observed. However, the problem considered herein does not include, for instance, the surface tension influence on the drop growth rate.

2.9 Third-order terms

Another possible improvement to the algorithm comes from the inclusion of the third-order terms in the modified equation analysis, which leads to the following form of the antidiffusive velocity (Margolin and Smolarkiewicz, 1998):

$$
\begin{aligned}
GC^{(k)}_{i+\frac{1}{2}} \rightsquigarrow GC^{(k,\text{tot})}_{i+\frac{1}{2}} &= GC^{(k)} + B_i \cdot GC^{(k)}_{i+\frac{1}{2}} \times \\
&\times \frac{1}{6}\left(4\frac{|GC^{(k)}_{i+\frac{1}{2}}|}{G_{i+1}+G_i} - 8\left(\frac{GC^{(k)}_{i+\frac{1}{2}}}{G_{i+1}+G_i}\right)^2 - 1\right)
\end{aligned} \qquad (2.22)
$$

$$
\begin{aligned}
B_i = &2 \cdot (\psi^*_{i+2} - \psi^*_{i+1} - \psi^*_i + \psi^*_{i-1}) \times \\
&\times \begin{cases} (1+1+1+1)^{-1} & (iga) \\ (\psi^*_{i+2}+\psi^*_{i+1}+\psi^*_i+\psi^*_{i-1})^{-1} & (else) \end{cases}
\end{aligned} \qquad (2.23)
$$

Figure 7 depicts how enabling the third-order-terms improves the solution of the test problem with respect to the upwind and basic MPDATA.

Noteworthy, discussion of higher-order variants of MPDATA was carried forward in Kuo et al. (1999) and Waruszewski et al. (2018). In the latter case, the focus was placed on accounting for coordinate transformation and variable velocity in the derivation of antidiffusive velocities leading to a fully third-order accurate scheme.

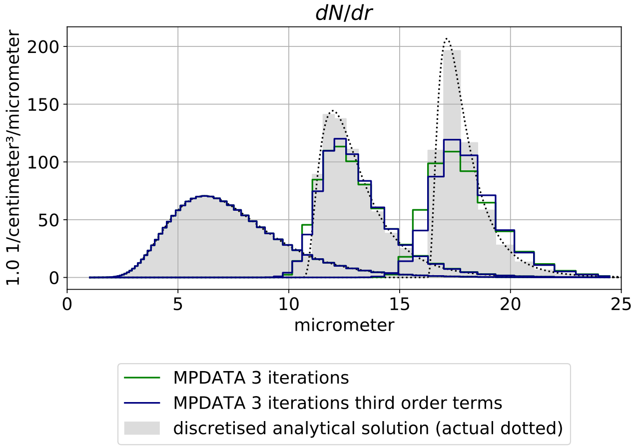

Figure 7. Comparison of analytic, upwind and MPDATA solutions (see plot key for algorithm variant specification) using the setup from Fig. 1, see sec. 2.9 for discussion.

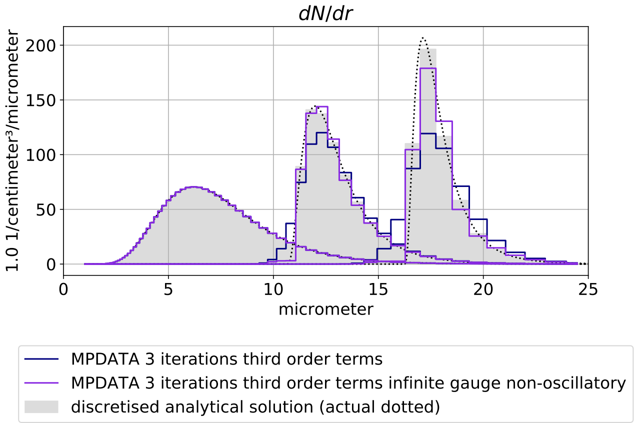

Figure 8. Comparison of analytic, upwind and MPDATA solutions (see plot key for algorithm variant specification) using the setup from Fig. 1, see sec. 2.10 for discussion.

2.10 A "best" combination of options

The MPDATA variants presented in the preceding sections can be combined together. In Figure 8, results obtained with the upwind scheme and the basic two-pass MPDATA are compared to those obtained with a combination of three iterations, third-order-terms, infinite-gauge and non-oscillatory options hereinafter referred to as the "best" variant (for the problem at hand).

In the following subsections, the influence of MPDATA algorithm variant choice on the resultant spectrum broadness and computational cost is analysed using the example simulation setup used above (i.e., in all figures except Fig. 2, see section 2.2 for test case definition).

Table 1. Relative dispersion of the discretised (using grid setup as in Fig. 1) analytical solution taken for five selected times.

Variant	d_{analytic}
$d(M=1\,\text{g}\,\text{kg}^{-1})$	0.357
$d(M=2\,\text{g}\,\text{kg}^{-1})$	0.202
$d(M=4\,\text{g}\,\text{kg}^{-1})$	0.126
$d(M=6\,\text{g}\,\text{kg}^{-1})$	0.097
$d(M=8\,\text{g}\,\text{kg}^{-1})$	0.080
$d(M=10\,\text{g}\,\text{kg}^{-1})$	0.069

Analysis of the scheme solution convergence with changing resolution and Courant number is presented in Appendix A.

2.11 Quantification of numerical broadening

The relative dispersion, defined as the ratio of standard deviation σ to the mean μ of the spectrum, is a parameter commonly used to describe the width of the spectrum (e.g. Chandrakar et al., 2018).

The calculated dispersion ratio over all bins takes form:

$$d = \frac{\sqrt{\frac{1}{N}\sum_i m_i^{(l=2)} - \left(\frac{1}{N}\sum_i m_i^{(l=1)}\right)^2}}{\frac{1}{N}\sum_i m_i^{(l=1)}} \tag{2.24}$$

where m_i is defined in (2.6) and N is the conserved total number of particles (equal to $\sum_i m_i^{(l=0)}$). To quantify the effect of numerical diffusion on the broadness of the resultant spectrum, the following parameter is introduced based on the numerical and analytical solutions (hereinafter reported in percentages):

$$R_\text{d} = d_\text{numerical}/d_\text{analytical} - 1 \tag{2.25}$$

Table 1 depicts the gradual narrowing of the spectrum under undisturbed adiabatic growth.

Left panel in Fig. 9 provides values of the R_d parameter evaluated at six selected timesteps corresponding to $M = 1,2,4,6,8,10\ \text{g}\,\text{kg}^{-1}$. Although numerical broadening is inherent to all employed schemes and grows in time for all considered variants, the scale of the effect is significantly reduced when using MPDATA.

In particular, a tenfold decrease in numerical broadening as quantified using R_d is observed comparing upwind and the "best" variant considered herein.

2.12 Notes on conservativeness

Due to the formulation of the problem as number conservation and discretisation of the evolution equation using fixed bins, even though the numerical scheme is conservative (up to subtle limitations outlined below), evaluation of other statistical moments of the evolved spectrum from the number

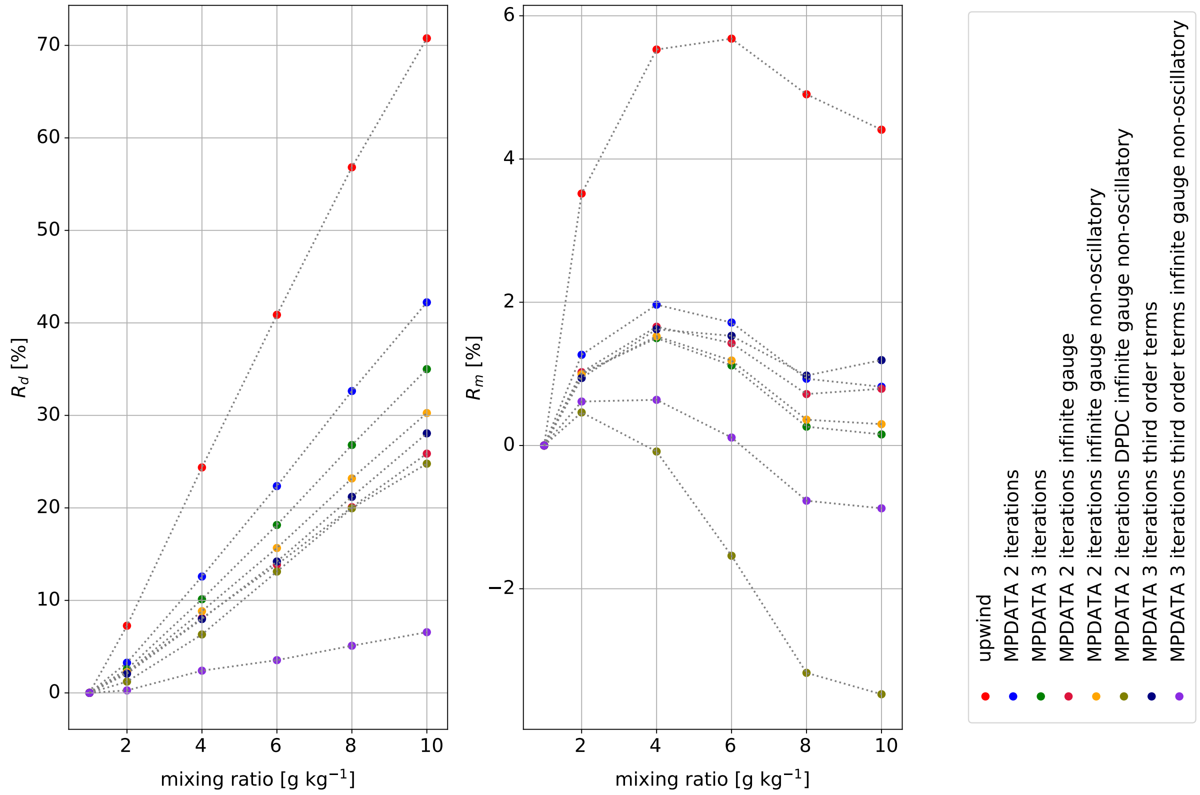

Figure 9. Left panel summarises values of the numerical-to-analytical spectral width ratio $R_\mathrm{d} = d_\mathrm{numerical}/d_\mathrm{analytical} - 1$ (expressed as a percentage) computed for simulations using different discussed variants of MPDATA and plotted as a function of increasing mixing ratio (i.e., each simulation is depicted with a set of line-connected points corresponding to selected timesteps), see section 2.11. Right panel presents analogous analysis for R_m, see section 2.12 for discussion. Note: $R_M = R_d = 0$ corresponds to perfect match with the analytical solution.)

density introduces an inherent discrepancy from the analytical results (for a discussion on multi-moment formulation of the problem, see e.g. Liu et al., 1997).

In order to quantify the discrepancy in the total mass between the discretised analytical solution and the numerically integrated spectrum, the following ratio is defined using moment evaluation formula (2.6):

$$R_M = M^{(\text{numeric})}/M^{(\text{analytic})} - 1 = \\ = \frac{\sum_i m_i^{(l=3,\ \text{numeric})}}{\sum_i m_i^{(l=3,\ \text{analytic})}} - 1. \qquad (2.26)$$

The right panel in Fig. 9 depicts the values of the above-defined ratio computed for spectra obtained with different variants of MPDATA discussed herein. The departures from analytically-derived values are largest for the upwind scheme (up to ca. 5%) and oscillate around 0 with an amplitude of the order of 1% for most of the MPDATA solutions.

The consequences of mass conservation inaccuracies in the fixed-bin particle-size spectrum representation may not be as severe as in, e.g. dynamical core responsible for the transport of conserved scalar fields. The outlined discrepancies may be dealt with by calculating the change in mass during a timestep from condensation, then using it in vapour and latent heat budget calculations so the total mass and energy in the modelled system are conserved.

The problem embodied in equation (1.1) is the conservation of the number of particles and the embraced algorithm (2.1)-(2.2) is conservative (up to numerical precision) for $G = 1$. However, the formulation of the donor cell scheme $\psi^{n+1} = \psi^n + G_i^{-1}\left(F_{i-1/2} + F_{i+\frac{1}{2}}\right)$ on the staggered grid with $G \neq 1$, for example due to employment of non-identity coordinate transformations implies that even though the influx and outflux across boundary of adjacent cells is equal, discretisation of G_i at cell centres limits the level of accuracy in number conservation.

The total number of particles in the system may diverge from the analytical expected value even for the initial condition depending on the employed discretisation approach. In the present work, the probability density function is probed at cell centres effectively assuming piecewise-constant number density function. An alternative approach is to discretise the initial probabilities by assigning to ψ_i the values of $(\phi_{i+\frac{1}{2}} - \phi_{i-1/2})/(r_{i+\frac{1}{2}} - r_{i-1/2})$ where ϕ is the cumulative distribution.

Table 2. Wall times normalised with respect to the upwind solution compared to data reported in four earlier works: S83 denotes Smolarkiewicz (1983) (two-dimensional problem); SS05 corresponds to Smolarkiewicz and Szmelter (2005) (three-dimensional, unstructured grid); SR91 denotes Smolarkiewicz and Rasch (1991) and MSS00 corresponds to Margolin et al. (2000) (both reported for two-dimensional problems).

Variant		S83	SS05	SR91	MSS00
upwind	1.0	1.0	1.0	1.0	1.0
2 iters	2.5	2.9	4.3	5.4	3.7
2 iters, iga	2.2	-	1.9	-	-
2 iters, iga, non-osc	5.9	-	3.9	-	-
DPDC, iga, non-osc	6.2	-	-	-	-
3 iters	5.7	5	-	9.8	-
3 iters, tot	4.1	-	-	19	-
3 iters, tot, iga, non-osc	11	-	-	-	-

2.13 Computational cost

Table 2 includes an assessment of the relative computational cost of the explored variants of MPDATA. The performance was estimated by repeated measurements of the wall time and selecting the minimal value as representative. Values are reported after normalisation with respect to upwind times. Simulations were performed using the mass doubling grid.

The table includes, where available, analogous figures reported in earlier studies on MPDATA (see caption for comments on the dimensionality of the employed cases). Among notable traits is the decrease in computational cost when enabling the infinite gauge option what is associated with a reduced number of terms in both the flux function as well as in the antidiffusive velocity formulation (see section 2.5 in Hill, 2011, and sections 2.5-2.6 herein). The “best” variant is roughly ten times more costly than the upwind scheme for the case studied herein. Among studies of bin microphysics schemes, analogous measures were reported in Liu et al. (1997) where the variational method presented there was reported to execute 3.1 times longer than first-order upwind; and in Onishi et al. (2010) where the studied semi-Lagrangian scheme was reported to be characterised by over 4 times higher computational cost than upwind (see Table 4 therein). In the latter case, a direct comparison is hindered by significantly different stability constraints on the timestep.

Although the discussed problem is one-dimensional, a computationally efficient and an accurate solution is essential, as it typically needs to be solved at every timestep and grid point of a three-dimensional cloud model. While the reported upwind-normalised wall times give a rough estimation of the cost increase associated with a particular MPDATA option, the actual footprint on a complex simulation system will depend on numerous implementation details including parallelisation strategy.

3 Spectral-spatial advection with MPDATA (single-column test case)

3.1 Problem statement

In multidimensional simulations in which the considered particle number density field is not only a function of time and particle size, but also of spatial coordinates, there are several additional points to consider applying MPDATA to the problem.

First, in the context of atmospheric cloud simulations, owing to the stratification of the atmosphere, the usual practice is to reformulate the conservation problem in terms of specific number concentration being defined as the number of particles n_p (cf. eq. (1.1)) divided by the mass of air (commonly the dry air) effectively resulting in multiplication of the G factor (cf. eqs (1.2)-(2.1)) by the (dry) air density. This translates to maintaining a constant specific number concentration (summed across all particle-size categories) along the vertical dimension despite the presence of an air density gradient. Ordinary particle volume concentration would vary due to variable density of air (i.e., expansion of air along the vertical coordinate). Note, however, that in eq. (2.1) it is assumed that the G factor does not vary in time.

Second, even with a single spatial dimension (single-column setup), the coupled size-spectral/spatial advection problem is two-dimensional. This is where the inherent multidimensionality of MPDATA (also, the "M" in MPDATA) requires further attention. The one-dimensional antidiffusive formulæ discussed in sections 2.4-2.9 need to be augmented with additional terms representing cross-dimensional contributions to the numerical diffusion. For an introduction, see e.g. Section 2.2 in Smolarkiewicz and Margolin (1998), for original derivation see Smolarkiewicz (1984), for a recent work discussing the interpretation of all terms in the antidiffusive velocity formulæ, including cross-dimensional terms, see Waruszewski et al. (2018).

Third, in any practical application where the drop size evolution is coupled with the water vapour budget (and hence with supersaturation evolution), it is essential to evaluate the total change in mass of liquid water due to condensation which is then to be used to define the source term of the water vapour field (and in latent heat budget representation). Noteworthy, knowing the difference of values at $\mathrm{n}+1$ and at n timesteps of the advected specific number concentration field is not sufficient to evaluate the vapour sink/source term. This is because only the fluxes across the size-spectral dimension need to be accounted for (note that the fluxes in all MPDATA iterations need to be summed up).

Several recent papers are highlighting the need for scrutiny when comes to the interplay of size-spectral and spatial advection and the associated numerical broadening (Morrison et al., 2018; Hernandéz Pardo et al., 2020; Lee et al., 2021). In the following subsection, a set of single-column simulations is presented and discussed depicting the performance of

MPDATA in a size-spectral/spatial advection problem coupled with vapour advection and supersaturation budget. The simulations are performed using a commonly employed MPDATA setting with only the non-oscillatory option enabled, and the discussion is focused on the sensitivity of the results to spatial, spectral and temporal resolution, as well as to the effect of performing one or two corrective passes of MPDATA (two or three iterations, respectively).

3.2 Test case definition

The test setup is based on the single-column KiD warm case introduced in Shipway and Hill (2012). This prescribed-flow framework has been further used, e.g., in Field et al. (2012) (mixed-phase scenario), in Hill et al. (2015) (warm rain scenario), in Gettelman and Morrison (2015) (both pure-ice, mixed-phase and warm-rain scenarios) and in the Hill et al. (2021) microphysics models intercomparison study (warm rain scenario). Here, condensation is the only microphysical process considered.

The simulated 3.2 km height column of air is described by: a constant-in-time piecewise-linear potential temperature profile (297.9 K from the ground to the level of 740 m, linearly decreasing down to 312.66 K at 3260 m); constant-in-time hydrostatic pressure and density profiles computed assuming surface pressure of 1007 hPa; piece-wise linear initial vapour mixing ratio profile ($15\ \mathrm{g\,kg^{-1}}$ at ground, $13.8\ \mathrm{g\,kg^{-1}}$ at 740 m and $2.4\ \mathrm{g\,kg^{-1}}$ at 3260 m); and a constant-in-space but time-dependent vertical momentum defined by $\rho_d w(z,t) = \rho_d w_1 \sin(\pi t/t_1)(1-H(t-t_1))$ where H is the Heaviside step function, w is the vertical velocity, $w_1 = 2.5\,\mathrm{m\,s^{-1}}$, ρ_d is the hydrostatic dry density profile and $t_1 = 600$ s. Note that the vertical velocity thus differs from the original KiD setup where w is held constant, the change is motivated by the aim of maintaining the non-divergent flow field condition.

The advection is thus solved for two scalar fields: (i) a one-dimensional field representing vertical variability of water vapour mixing ratio (mass of vapour per mass of dry air) and (ii) a two-dimensional field representing vertical and spectral variability of liquid particle specific concentration (number of particles per mass of dry air). The spectral coordinate is set to particle radius ($p = r$) and the bins are laid out uniformly ($x = r$) over a range of 1 μm to 20.2 μm. Noteworthy, this results in the size-spectral component of the advection velocity being divergent (while the vertical component is non-divergent).

The initial condition does not feature supersaturation anywhere in the domain. The upward advection of water vapour causes supersaturation to occur and trigger condensation. The size-spectral velocity is defined as in the box-model test case (cf. eq. (2.3)) but with supersaturation being time-dependent and derived from the values of vapour mixing ratio, temperature and pressure at a given level. Note that the temperature profile is constant in time and the test case does not feature representation of latent heat release effects, only the ambient air/particle vapour budget is accounted for by subtracting the amount of condensed water from the vapour field in each timestep, before performing the subsequent step of advection on the vapour mixing ratio field.

The domain is initially void of liquid water and the only source of it is through the boundary condition in the spectral dimension specified as follows:

$$\psi_{-1} = \max\left(0, N_{\mathrm{CCN}} - \sum_i \psi\right) \tag{3.1}$$

with $i = -1$ denoting the halo grid cell at the left edge of the spectral domain on a given vertical level and the summation spans all bins at a given level (excluding halo grid cells). The flux across the domain boundary in the spectral dimension represents the cloud droplet activation. The flux is dependent, through eq. (2.3) on the supersaturation at a given level, and on the N_{CCN} parameter representing a maximal number of activated droplets (per unit mass of dry air). In the performed simulations, N_{CCN} was set to 500 $\mathrm{mg^{-1}}$. For discussion of other ways to represent activation in bin microphysics models, see, e.g., Grabowski et al. (2011).

The simulations are run for 15 minutes out of which the first 10 involve non-zero vertical velocity (as $t_1 = 600$ s).

3.3 Discussion of results

Figure 10 depicts qualitatively how MPDATA performs with the single-column simulation depending on the number of MPDATA iterations employed. Presented simulation, hereinafter referred to as base resolution case, is performed with the liquid water dynamics resolved on a 32×32 grid with a vertical grid step $\Delta z = 100$ m, size-spectral grid step $\Delta r = 0.6$ μm and timestep $\Delta t = 0.25$s. The two-dimensional liquid water mixing ratio grid is rendered with a shaded array of histogram bars. The vertical axis corresponds to the advected quantity: spatio-spectral number density divided by the dry density of air. Histogram bars with values of less than 1% of the vertical axis range ($1\% \times 2$ $\mathrm{m^{-1}mg^{-1}\mu m^{-1}}$) are not plotted for clarity. Presented plots are aimed at intuitively portraying the model state and the extent to which the introduction of subsequent MPDATA corrective iterations counteracts the numerical spectrum broadening. Note that besides the depicted liquid water mixing ratio, the model state consists as well of a one-dimensional vapour mixing ratio vector.

In Figure 11, the base resolution case is depicted with plots constructed following the original methodology from Shipway and Hill (2012) (as in Fig. 1 therein). The grey-scale maps depict the evolution in time and vertical dimension of water vapour mixing ratio q_l, supersaturation S and the droplet spectrum relative dispersion d. The adjacent profile plots depict the vertical variability of the mapped quantity at four selected times.

Notwithstanding the highly idealised and simplified modelling framework employed herein, one may attempt a com-

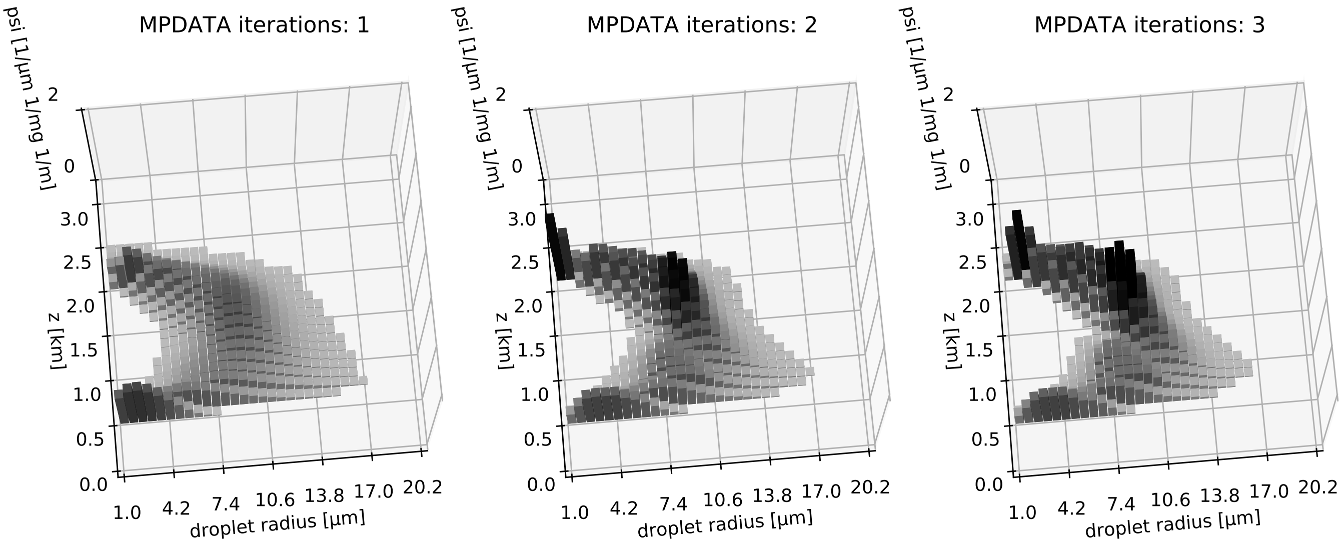

Figure 10. Snapshots of the advected two-dimensional liquid water field at $t = t_1 = 600$s for three different number of iterations settings of MPDATA (with the non-oscillatory option enabled).

parison with profiles obtained from both in-situ aircraft measurements (Arabas et al., 2009, profiles of d in Fig. 1 therein) and detailed three-dimensional simulations (Arabas and Shima, 2013, profiles of S and liquid water content in Fig. 2-4 therein) inspired by the same RICO field campaign (Rauber et al., 2007) as the single-column setup of Shipway and Hill (2012). The comparison merely confirms that the chosen test case covers the parameter space relevant to the studied problem. Resemblance remains, at most, qualitative, as expected given the stark simplicity of the KiD framework. Interestingly, the parabolic vertical profile of the relative dispersion obtained herein was also reported in Lu and Seinfeld (2006) for bin-microphysics three-dimensional simulations of marine stratocumulus. In the discussion of figures 2, 3 & 6 therein, it was hypothesised that the parabolic shape is a signature of entrainment as well as updraft-downdraft interactions, none of which are represented in the kinematic framework employed herein.

The liquid water profiles depicted in the top row of Fig. 11 reveal that the cloud structure developed within the first ca. 9 minutes of the simulation is later maintained, with the profiles at $t = 9$ min. and $t = 12$ min. being virtually indistinguishable. Middle row plots of supersaturation profiles depict that the considered simulation setup enables to capture of the characteristic supersaturation maximum just above cloud base. Furthermore, it is evident that the corrective iterations of MPDATA influence the maximal supersaturation values. Noteworthy, this results in different timestep (Courant number) constraints depending on the number of iterations used because the spectral velocity is a function of supersaturation.

There is a cloud-top activation feature hinted in all three panels in Fig. 10 as well as indirectly in the supersaturation profiles in Fig. 11. The representation of activation above cloud base is sensitive to both numerical details of vapour and heat transport reflected in the diagnosed supersaturation as well as to the assumptions behind the activation formulation itself (see e.g. discussion of Fig. 2 and Fig. 6 in Slawinska et al., 2012, and references therein). Given the simplified treatment of activation defined by eq. (3.1), together with the unphysical assumption of constant temperature profile, the only conclusion here is that the visualisation method used in Fig. 10 is apt to highlight this feature. Noteworthy, what is consistent with the differences in supersaturation values between upwind and MPDATA solutions, the effect is in fact unnoticeable in the case of the upwind solution presented in Fig. 10.

The bottom row in Fig. 11 depicts the relative dispersion defined and computed as in section 2.11, discarding levels where the total droplet number mixing ratio summed over all bins on a level is below 5% of N_{CCN}. Narrowing of the spectrum with a height below $z = 1.5$ km depicted by decreasing values of d is a robust feature. Minimal values of d vary visibly depending on the number of MPDATA iterations employed.

To provide insight into the sensitivity of the results to temporal, spatial and spectral resolution, Fig. 12 presents the relative dispersion profiles at $t = t_1 = 10$ min. for several resolution settings. In the background of the figure, there are three axes plotted pointing the directions in which the figure panels can be explored to reveal the dependence on: the vertical spatial spacing Δz (left-to-right), the spectral spacing Δr (bottom-to-top), and the timestep (back-to-foreground). The base resolution case is plotted at the intersection of the background axes. Note that besides the back-to-foreground sequence of plots where all but the timestep settings is kept

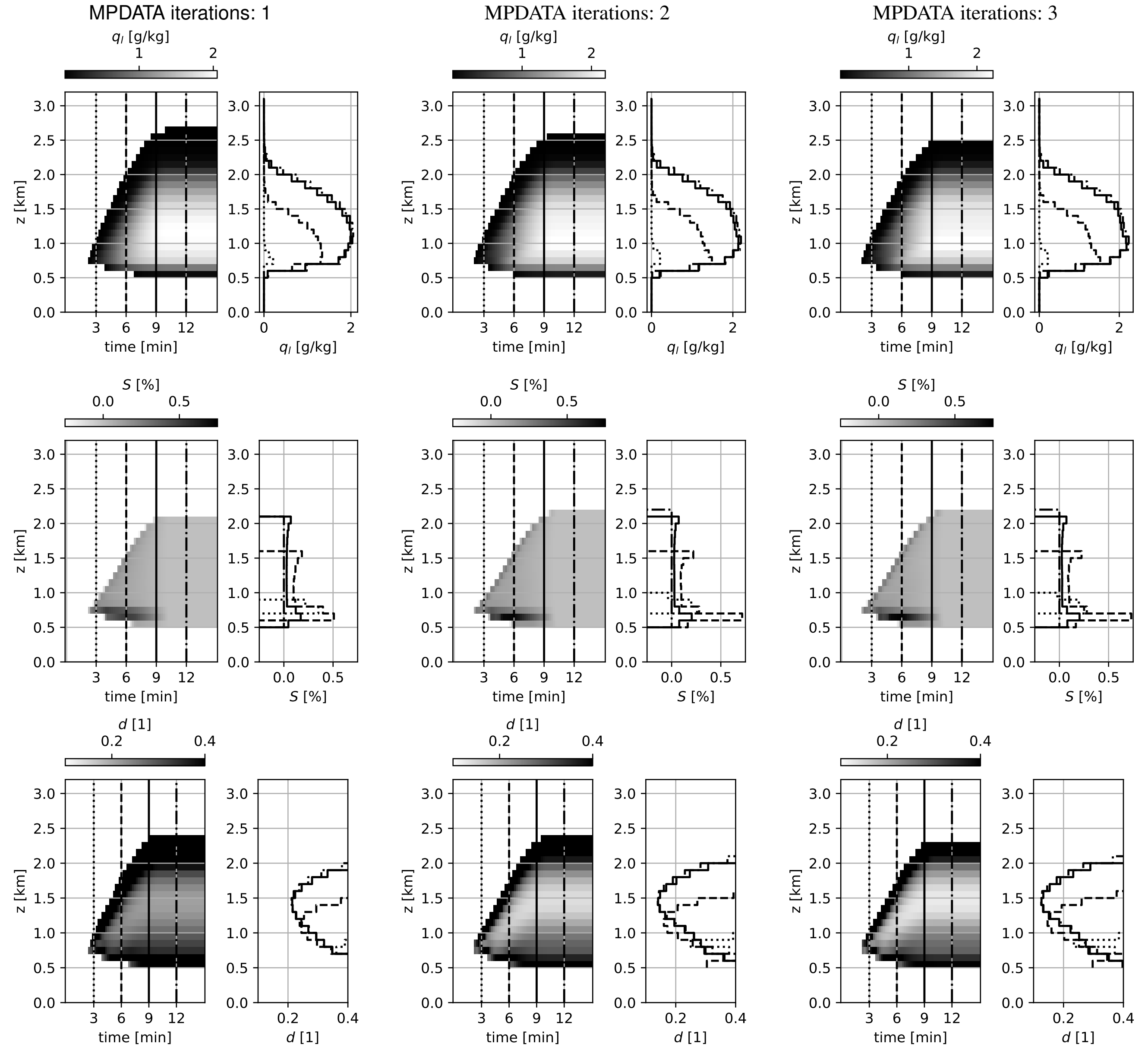

Figure 11. Single-column simulations depicted with three selected variables: liquid water mixing ratio q_l (top row), supersaturation S (middle row) and relative dispersion d (bottom row); for three settings of the iteration count in MPDATA (one iteration corresponding to the basic upwind scheme, left column). Each of nine datasets (three iteration settings, three variables) is plotted with a grey-scale time vs. altitude map (left panels with the colour scale above) and a set of four profiles (right panels). Profiles are plotted for $t = 3$ min. (dotted), 6 min. (dashed), 9 min. (solid), & 12 min. (dash-dot), with vertical lines of corresponding line style plotted at given times in the left panels. For plotting, the model state is resampled by averaging in the time dimension to reduce the number of plotted steps by a factor of 50 (from 3600 down to 72).

equal, the timestep also varies with the grid settings to fulfil scheme stability constraint.

The dependence on the temporal resolution, as gauged by comparing the base resolution case with cases with the timestep halved ($\Delta t = 125$ ms; background) and doubled ($\Delta t = 500$ s; foreground), is barely observable. This is in general agreement with Morrison et al. (2018) and Hernandéz Pardo et al. (2020) where the dependence on timestep is shown to be much smaller than on the spatial or spectral resolution.

The dependence on the spectral resolution is captured and clearly manifested at the lowest spectral resolution where the minimal spectral dispersion d drops by ca. 0.1 when decreasing $\Delta r = 1.2\mu$m down to $\Delta r = 0.3\mu$m. Little further change can be observed by refining the resolution down to $\Delta r = 0.15\mu$m. Focusing on the minimal values of d for a

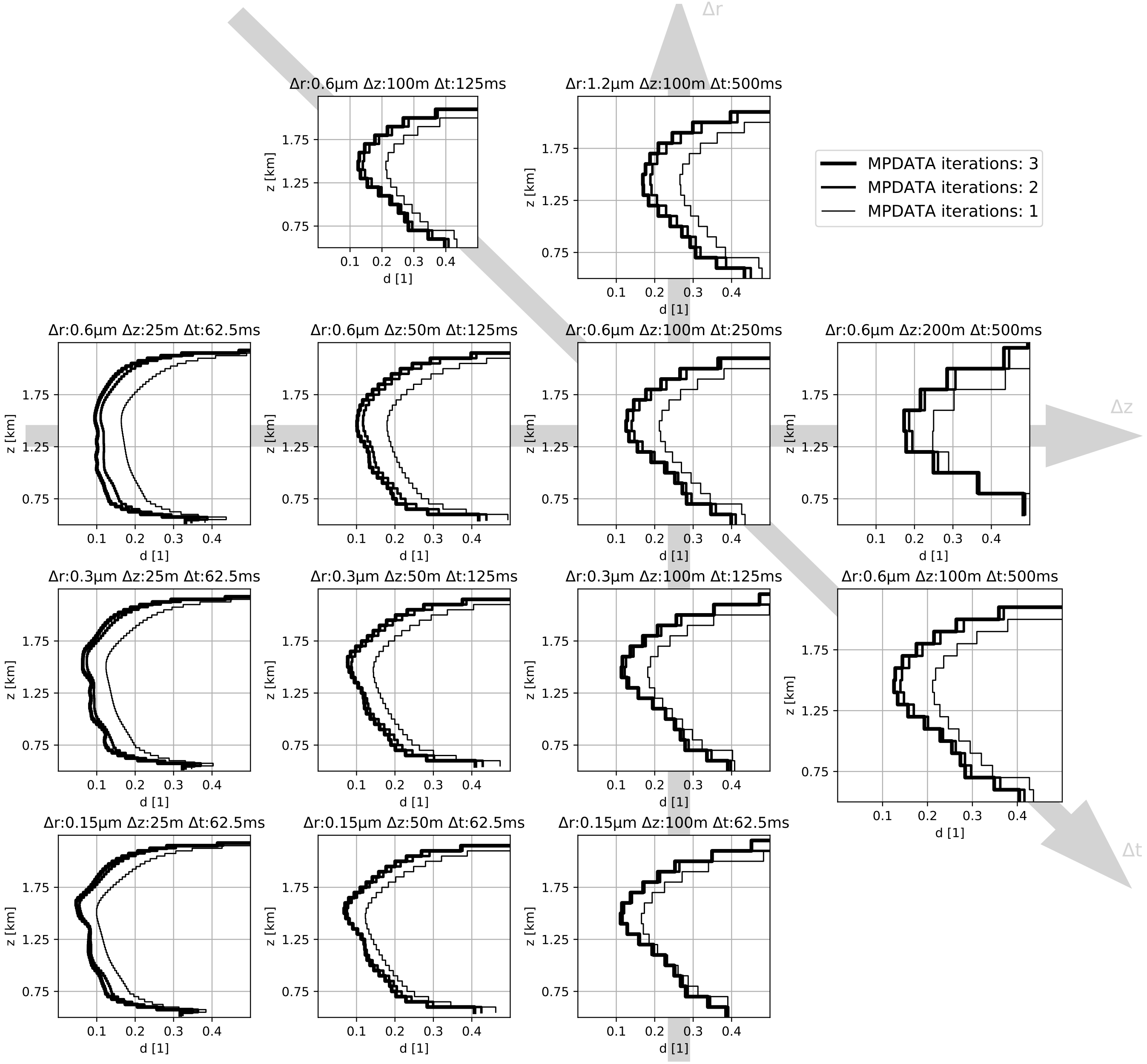

Figure 12. Profiles of relative dispersion d for a set of temporal, spatial and spectral resolution settings (Δr, Δz and Δt values given in labels above each plot). Each panel depicts results for three different MPDATA iteration counts (one iteration corresponding to the basic upwind scheme). Profiles plotted for $t = t_1 = 10$ min.

given profile, in general, the lower the spectral resolution, the more profound the effect of introducing corrective iterations of MPDATA. In most cases, applying even a single corrective step (i.e., 2 iterations) results in halving of the minimal values d as compared to the upwind solution (i.e., 1 iteration).

The spatial resolution setting Δz significantly alters the results, particularly near the cloud base. The values of d at the lower half of the presented profile (i.e., ca. below $z = 1$ km) drop from over 0.3 down to around 0.1 when refining the resolution from $\Delta z = 200$ m down to $\Delta z = 25$ m.

4 Conclusions

The study was focused on the MPDATA family of numerical schemes and its application to the size-spectral as well as spatio-spectral transport problem arising in models of condensational growth of cloud droplets. MPDATA iteratively applies the upwind algorithm, first with the physical velocity, subsequently using antidiffusive volocities. As a result, the algorithm is characterised by reduced numerical diffusion while maintaining the salient features of the underlying upwind scheme such as conservativeness and positive-definiteness.

In literature, the derivation and discussion of MPDATA variants are spread across numerous research papers published across almost four decades, and in most cases focused on multidimensional hydrodynamics applications. It was the aim of this study, to highlight the developments that followed the original formulation of the algorithm, and to highlight their applicability to the problem. To this end, it was shown that the combination of such features of MPDATA as the infinite-gauge, non-oscillatory and third-order-terms options, together with the application of multiple corrective iterations offer a robust scheme that grossly outperforms the almost quadragenarian basic MPDATA. The procedure to introduce coordinate transformations, e.g., to a mass-doubling grid in the context of size-spectral transport was detailed.

In the case of the single-column test case, the simulations featured coupling between droplet growth and supersaturation evolution. The cloud droplet spectrum relative dispersion is influenced by numerical diffusion pertinent to both spectral and vertical advection. Focusing on the levels corresponding to the region of maximal liquid water content (ca. between $z = 1$ km and 2 km for the case considered), it was shown that application of even a single corrective iteration of MPDATA robustly reduces (in most cases more than halves) the spectral width. In agreement with conclusions drawn from single-column simulations in Morrison et al. (2018) and Lee et al. (2021), within the range of explored grid settings, the vertical resolution has the most profound effect on the overall characteristics of the spectrum width profile as it significantly influences the just-above-cloud-base evolution of the spectral width.

Code availability. The calculations are performed using Python with a new open-source implementation of MPDATA: PyMPDATA (Bartman et al., 2021). In terms of numerics, PyMPDATA closely follows libmpdata++ (Jaruga et al., 2015).

All of presented figures and tables can be recreated in interactive notebooks "in the cloud" using the mybinder.org or Colab platforms. To launch the notebooks, follow the links: https://github.com/atmos-cloud-sim-uj/PyMPDATA-examples/tree/main/PyMPDATA_examples/Olesik_et_al_2020 and https://github.com/atmos-cloud-sim-uj/PyMPDATA-examples/tree/main/PyMPDATA_examples/Shipway_and_Hill_2012. The notebooks are part of the PyMPDATA-examples Python package. Both PyMPDATA and PyMPDATA-examples are licensed under the GNU General Public License 3.0, are available on the PyPI.org Python package repository, and are additionally enclosed as an electronic supplement to this paper.

The single-column framework is a Python reimplementation of the open-source KiD code available at https://github.com/BShipway/KiD.

Appendix A: Convergence analysis

To assess the spatial and temporal convergence of the numerical solutions presented above, a convergence test originating from Smolarkiewicz and Grabowski (1990) is used. For the analysis the following truncation-error L^2 measure is used (e.g., Smolarkiewicz, 1984):

$$\mathrm{Err}_{L2} = \frac{1}{T}\sqrt{\sum_i \left(\psi_i^{\text{numerical}} - \psi_i^{\text{analytical}}\right)^2 / nx}. \tag{A1}$$

As a side note, it is worth pointing out that for the chosen coordinates $\left(p = r^2, x = r^2\right)$, the coordinate transformation term is equal to the identity, so there is no need for including the G factor into the computed error measures. In the general case, convergence will depend on the grid choice and to account for that one may use a modified measure as given in Smolarkiewicz and Rasch (1991, eq. 24).

To explore the convergence, the error measures are computed for 7 different linearly spaced values of C between 0.05 and 0.95, and $nx \in \left\{2^7, 2^8, 2^9, 2^{10}, 2^{11}, 2^{12}, 2^{13}, 2^{14}\right\}$ resulting in 56 simulations for each presented combination of options.

As proposed in Smolarkiewicz and Grabowski (1990), visualization of the results is carried out on polar plots with radius ρ and angle ϕ coordinates defined as follows:

$$\rho = \ln_2\left(\frac{1}{nx}\right) + \text{const}, \quad \phi = C\frac{\pi}{2}, \tag{A2}$$

where ρ was shifted by a constant so that the highest resolution grid corresponds to $\rho = 1$.

Figures A1-A8 depict the convergence rates and are intended for comparison with analogously constructed plots in Figs. 2-3 Smolarkiewicz and Grabowski (1990), Figs. 8.1-8.2 Margolin and Smolarkiewicz (1998) and Figs. 10-11 Jaruga et al. (2015).

The chosen colour increments correspond to the error reduction by a factor of 2, the warmer the colour, the larger the error. The small grey points behind the isolines represent points for which the error value was calculated. When moving along the lines of constant Courant number, increasing the space and time discretisation, the number of crossed dashed isolines indicate the order of convergence. For the considered problem, it can be seen that the upwind scheme (Fig. A1) has a convergence of the first order (one isoline is crossed when spatial discretisation increases by one order); MPDATA scheme (Fig. A2) of the second-order and MPDATA with 3 iterations (Fig. A6) is of the third order.

Moreover, the shape of the dashed isolines tells the dependency of the solution accuracy on the Courant number. When these are isotropic (truncation error being independent of polar angle), the solution is independent of the Courant number.

Noteworthy, in Fig. A3 and Fig. A4, s groove of the third-order convergence rate is evident around $\phi = \frac{\pi}{4}$, normally characteristic for MPDATA with three or more passes.

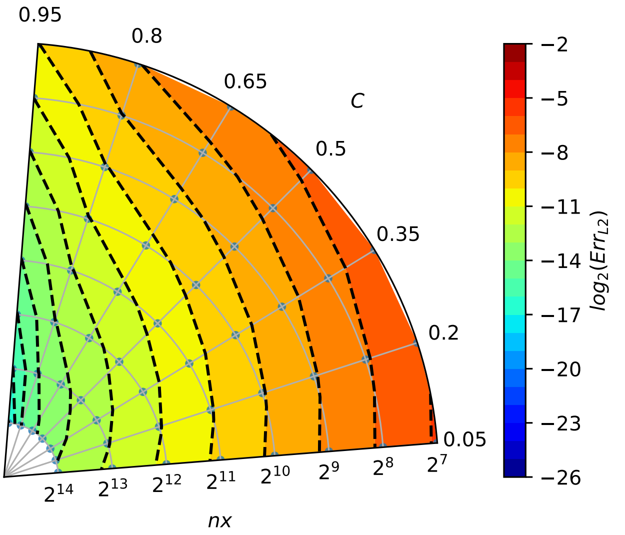

Figure A1. Convergence plot for the upwind scheme (cf. Fig. 1). Angle in the polar plot corresponds to the Courant number C; the distance from origin denotes the number of grid boxes nx, see eq. (A2). Grey dots indicate data point locations – parameter values for which computations were made. Colours and isolines depict the error measure values (interpolated from the data point locations), see eq. (A1).

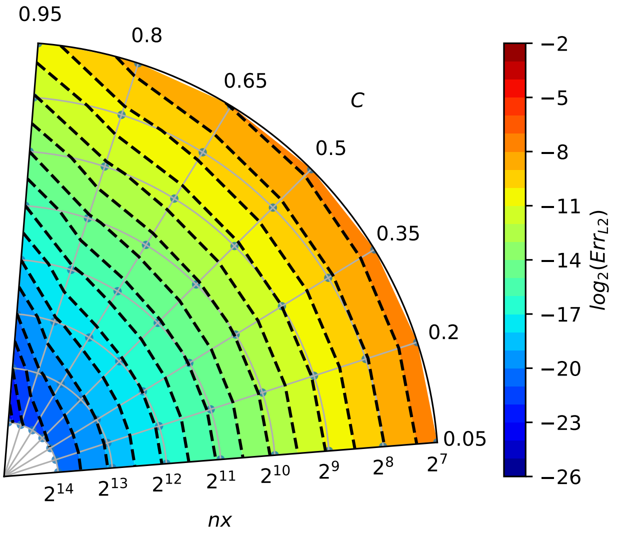

Figure A2. Convergence plot for basic two-pass MPDATA (cf. Fig. 3). See caption of Fig. A1 for the description of plot elements.

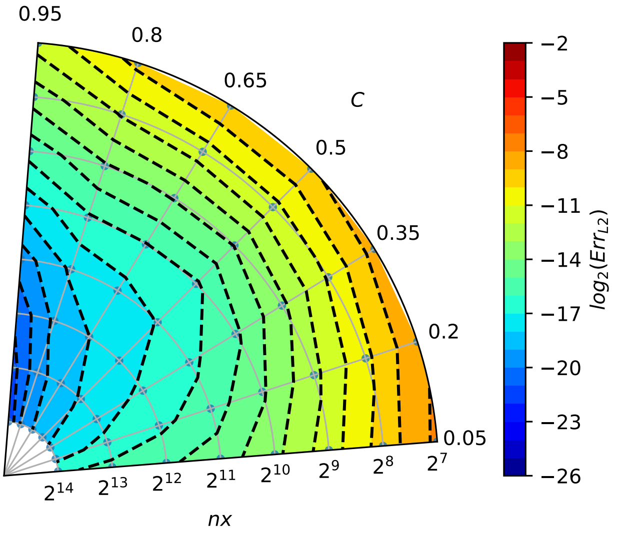

Figure A3. Convergence plot for the infinite gauge MPDATA (cf. Fig. 4). See caption of Fig. A1 for the description of plot elements.

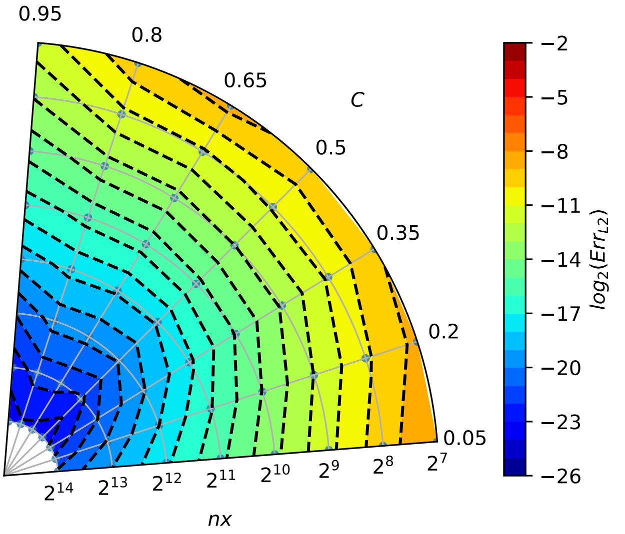

Figure A4. Convergence plot for the infinite gauge non-oscillatory variant of MPDATA (cf. Fig. 5). See caption of Fig. A1 for the description of plot elements.

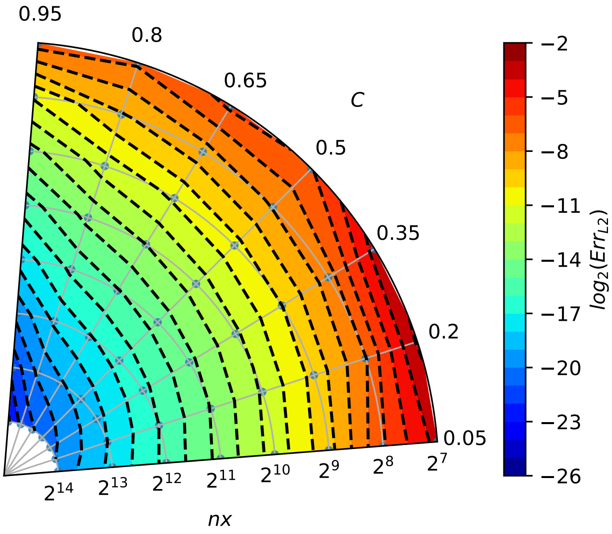

Figure A5. Convergence plot for the DPDC variant with infinite gauge and non-oscillatory corrections (cf. Fig. 6). See caption of Fig. A1 for the description of plot elements.

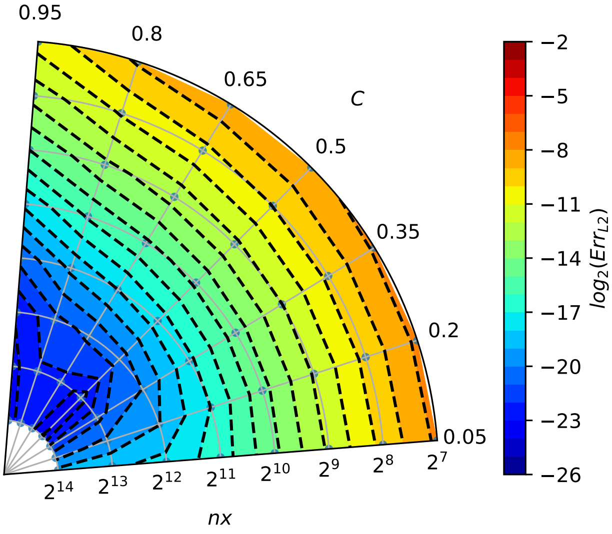

Figure A7. Convergence plot for the three-pass MPDATA with third-order terms (cf. Fig. 7). See caption of Fig. A1 for the description of plot elements.

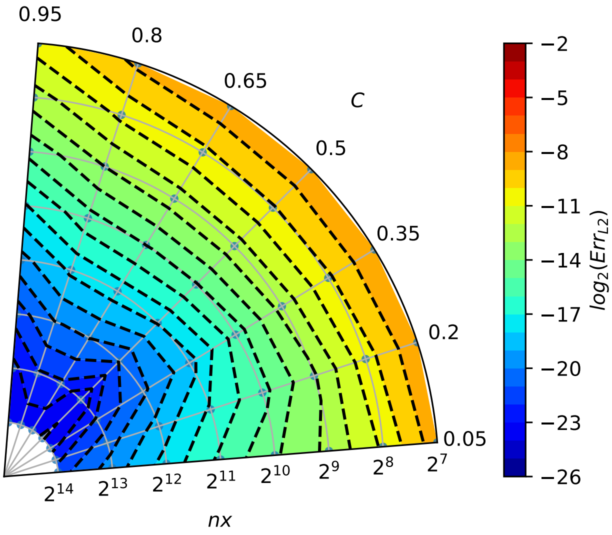

Figure A6. Convergence plot for the three-pass MPDATA (cf. Fig. 3). See caption of Fig. A1 for the description of plot elements.

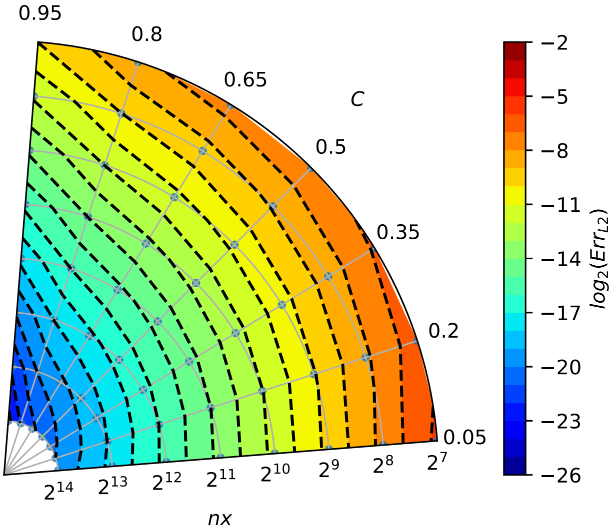

Figure A8. Convergence plot for the three-pass infinite gauge non-oscillatory MPDATA with third-order term corrections (cf. Fig. 8). See caption of Fig. A1 for the description of plot elements.

When second-order truncation error is sufficiently reduced, the third-order error, proportional to $(1-3C+2C^2)$ as can be seen in (2.22), dominates, but vanishes for $C=0.5$, thus resulting in the existence of the groove.

The convergence test results for the three-pass MPDATA with infinite gauge, non-oscillatory and third-order terms options enabled (Fig. A8) are consistent with results depicted in Fig. A7, although the order of convergence is reduced due to the employment of non-oscillatory option.

Author contributions. The idea of the study originated in discussions between SA, SU and MO. MO led the work and preliminary version of a significant part of the presented material constituted his MSc thesis prepared under the mentorship of SA. PB architected the key components of the PyMPDATA package. JB contributed the DPDC variant of MPDATA to PyMPDATA. MB participated in composing the paper and devising the result analysis workflow. All authors contributed to the final form of the text.

Competing interests. The authors declare no competing interests. Simon Unterstrasser and Sylwester Arabas are members of the editorial board of Geoscientific Model Development. The peer-review process has been handled by an independent editor.

Acknowledgements. Comments from Wojciech Grabowski, Adrian Hill, Hugh Morrison, Andrzej Odrzywołek, Piotr Smolarkiewicz and Maciej Waruszewski as well as paper reviews by Josef Schröttle and three anonymous reviewers helped to improve the manuscript. The project was carried out within the POWROTY/REINTEGRATION programme of the Foundation for Polish Science co-financed by the European Union under the European Regional Development Fund (POIR.04.04.00-00-5E1C/18-00).

References

Abade, G., Grabowski, W. W., and Pawlowska, H.: Broadening of Cloud Droplet Spectra through Eddy Hopping: Turbulent Entraining Parcel Simulations, J. Atmos. Sci., 75, https://doi.org/10.1175/JAS-D-18-0078.1, 2018.

Arabas, S. and Pawlowska, H.: Adaptive method of lines for multi-component aerosol condensational growth and CCN activation, Geosci. Model Dev., 4, https://doi.org/10.5194/gmd-4-15-2011, 2011.

Arabas, S. and Shima, S.-I.: Large-Eddy Simulations of Trade Wind Cumuli Using Particle-Based Microphysics with Monte Carlo Coalescence, J. Atmos. Sci., 70, https://doi.org/10.1175/JAS-D-12-0295.1, 2013.

Arabas, S. and Shima, S.-I.: On the CCN (de)activation nonlinearities, Nonlin. Proc. Geophys., 24, https://doi.org/10.5194/npg-24-535-2017, 2017.

Arabas, S., Pawlowska, H., and Grabowski, W.: Effective radius and droplet spectral width from in-situ aircraft observations in trade-wind cumuli during RICO, Geophys. Res. Lett., 36, https://doi.org/10.1029/2009GL038257, 2009.

Bartman, P., Banaśkiewicz, J., Drenda, S., Manna, M., Olesik, M., Rozwoda, P., Sadowski, M., and Arabas, S.: PyMPDATA v1: Numba-accelerated implementation of MPDATA with examples in Python, Julia and Matlab, https://pypi.org/p/PyMPDATA, 2021.

Beason, C. W. and Margolin, L. G.: DPDC (double-pass donor cell): A second-order monotone scheme for advection, in: Fifth Nuclear Code Developers' Conference, https://www.osti.gov/servlets/purl/7049237, LLNL report UCRL-99731, 1988.

Brown, R.: A numerical study of radiation fog with an explicit formulation of the microphysics, Q. J. R. Meteorol. Soc., 106, https://doi.org/10.1002/qj.49710645010, 1980.

Chandrakar, K. K., Cantrell, W., and Shaw, R. A.: Influence of Turbulent Fluctuations on Cloud Droplet Size Dispersion and Aerosol Indirect Effects, J. Atmos. Sci., 75, https://doi.org/10.1175/JAS-D-18-0006.1, 2018.

Courant, R., Isaacson, E., and Rees, M.: On the solution of nonlinear hyperbolic differential equations by finite differences, Comm. Pure Appl. Math., 5, https://doi.org/10.1002/cpa.3160050303, 1952.

Cristiani, E.: Blending Brownian motion and heat equation, J. Coupled Syst. Multiscale Dyn., 3, https://doi.org/10.1166/jcsmd.2015.1089, 2015.

Crowley, W. P.: Numerical Advection Experiments, Mon. Weather Rev., 96, https://doi.org/10.1175/1520-0493(1968)096<0001:NAE>2.0.CO;2, 1968.

Devenish, B. J., Bartello, P., Brenguier, J.-L., Collins, L. R., Grabowski, W. W., IJzermans, R. H. A., Malinowski, S. P., Reeks, M. W., Vassilicos, J. C., Wang, L.-P., and Warhaft, Z.: Droplet growth in warm turbulent clouds, Q. J. R. Meteorol. Soc., 138, https://doi.org/10.1002/qj.1897, 2012.

Dhaniyala, S. and Wexler, A. S.: Numerical schemes to model condensation and evaporation of aerosols, Atmos. Env., 30, https://doi.org/10.1016/1352-2310(95)00288-X, 1996.

East, T. W. R.: An inherent precipitation mechanism in cumulus clouds, Q. J. R. Meteorol. Soc., 83, https://doi.org/10.1002/qj.49708335506, 1957.

East, T. W. R. and Marshall, J. S.: Turbulence in clouds as a factor in precipitation, Q. J. R. Meteorol. Soc., 80, https://doi.org/10.1002/qj.49708034305, 1954.

Field, P., Heymsfield, A., Shipway, B., DeMott, P., Pratt, K., Rogers, D., Stith, J., and Prather, K.: Ice in Clouds Experiment–Layer Clouds. Part II: Testing Characteristics of Heterogeneous Ice Formation in Lee Wave Clouds, J. Atmos. Sci., 69, https://doi.org/10.1175/JAS-D-11-026.1, 2012.

Gettelman, A. and Morrison, H.: Advanced Two-Moment Bulk Microphysics for Global Models. Part I: Off-Line Tests and Comparison with Other Schemes, J. Climate, 28, https://doi.org/10.1175/JCLI-D-14-00102.1, 2015.

Grabowski, W. and Wang, L.-P.: Growth of Cloud Droplets in a Turbulent Environment, Annu. Rev. Fluid Mech., 45, https://doi.org/10.1146/annurev-fluid-011212-140750, 2013.

Grabowski, W., Andrejczuk, M., and Wang, L.-P.: Droplet growth in a bin warm-rain scheme with Twomey CCN activation, Atmos. Res., 99, https://doi.org/10.1016/j.atmosres.2010.10.020, 2011.

Grabowski, W. W.: Comparison of Eulerian bin and Lagrangian particle-based microphysics in simulations of nonprecipitating cumulus, J. Atmos. Sci., https://doi.org/10.1175/JAS-D-20-0100.1, 2020.

Hall, W. D.: A Detailed Microphysical Model Within a Two-Dimensional Dynamic Framework: Model Description and Preliminary Results, J. Atmos. Sci., 37, https://doi.org/10.1175/1520-0469(1980)037<2486:ADMMWA>2.0.CO;2, 1980.

Hernandéz Pardo, L. H., Morrison, H., Machado, L. A. T., Harrington, J. Y., and Lebo, Z. J.: Drop Size Distribution Broadening Mechanisms in a Bin Microphysics Eulerian Model, J. Atmos. Sci., 77, https://doi.org/10.1175/JAS-D-20-0099.1, 2020.

Hill, A., Shipway, B., and Boutle, I.: How sensitive are aerosol-precipitation interactions to the warm rain representation?, J. Adv. Model. Earth Syst., 7, https://doi.org/10.1002/2014MS000422, 2015.

Hill, A., Lebo, Z., Andrejczuk, M., Arabas, S., Dziekan, P., Field, P., Gettelman, A., Hoffmann, F., Pawlowska, H., Onishi, R., and Vié, B.: Toward a numerical benchmark for warm rain processes, J. Atmos. Sci. (submitted), 2021.

Hill, R. N.: Numerical modelling of multi-material interfaces, Ph.D. thesis, Loughborough University, https://hdl.handle.net/2134/8103, 2011.

Hirt, C. W.: Heuristic stability theory for finite-difference equations, J. Comput. Phys., https://doi.org/10.1016/0021-9991(68)90041-7, 1968.

Howell, W.: The growth of cloud drops in uniformly cooled air, J. Meteorol., 6, https://doi.org/10.1175/1520-0469(1949)006<0134:TGOCDI>2.0.CO;2, 1949.

Hulburt, H. and Katz, S.: Some problems in particle technology: A statistical mechanical formulation, Chem. Eng. Sci., 19, https://doi.org//10.1016/0009-2509(64)85047-8, 1964.

Jaruga, A., Arabas, S., Jarecka, D., Pawlowska, H., Smolarkiewicz, P. K., and Waruszewski, M.: libmpdata++ 1.0: a library of parallel MPDATA solvers for systems of generalised transport equations, Geosci. Model Dev., 8, https://doi.org/10.5194/gmd-8-1005-2015, 2015.

Jeffery, C. A., Reisner, J. M., and Andrejczuk, M.: Another Look at Stochastic Condensation for Subgrid Cloud Modeling: Adiabatic Evolution and Effects, J. Atmos. Sci., 64, https://doi.org/10.1175/2006JAS2147.1, 2007.

Khain, A. P., Beheng, K. D., Heymsfield, A., Korolev, A., Krichak, S. O., Levin, Z., Pinsky, M., Phillips, V., Prabhakaran, T., Teller, A., van den Heever, S. C., and Yano, J.-I.: Representation of microphysical processes in cloud-resolving models: Spectral (bin) microphysics versus bulk parameterization, Rev. Geophys., 53, https://doi.org/10.1002/2014RG000468, 2015.

Kostinski, A. B. and Jameson, A. R.: On the Spatial Distribution of Cloud Particles, J. Atmos. Sci., 57, https://doi.org/10.1175/1520-0469(2000)057<0901:OTSDOC>2.0.CO;2, 2000.

Kostoglou, M. and Karabelas, A. J.: Evaluation of Numerical Methods for Simulating an Evolving Particle Size Distribution in Growth Processes, Chem. Eng. Comm., 136, https://doi.org/10.1080/00986449508936360, 1995.

Kovetz, A.: An Analytical Solution for the Change of Cloud and Fog Droplet Spectra Due to Condensation, J. Atmos. Sci., 26, https://doi.org/10.1175/1520-0469(1969)026<0302:AASFTC>2.0.CO;2, 1969.

Kovetz, A. and Olund, B.: The Effect of Coalescence and Condensation on Rain Formation in a Cloud of Finite Vertical Extent, J. Atmos. Sci., 26, https://doi.org/10.1175/1520-0469(1969)026<1060:TEOCAC>2.0.CO;2, 1969.

Kühnlein, C. and Smolarkiewicz, P. K.: An unstructured-mesh finite-volume MPDATA for compressible atmospheric dynamics, J. Comp. Phys., 334, https://doi.org/10.1016/j.jcp.2016.12.054, 2017.

Kuo, H.-C., Leou, T.-M., and Williams, R. T.: A study on the high-order Smolarkiewicz methods, Comput. Fluids, 28, https://doi.org/10.1016/s0045-7930(98)00036-x, 1999.

Lange, R.: ADPIC: a three-dimensional computer code for the study of pollutant dispersal and deposition under complex conditions, https://doi.org/10.2172/4308175, LLNL report no. UCRL-51462, 1973.

Lange, R.: ADPIC—A Three-Dimensional Particle-in-Cell Model for the Dispersal of Atmospheric Pollutants and its Comparison to Regional Tracer Studies, J. Appl. Meteorol., 17, https://doi.org/10.1175/1520-0450(1978)017<0320:ATDPIC>2.0.CO;2, 1978.

Lee, H., Fridlind, A., and Ackerman, A.: An Evaluation of Size-Resolved Cloud Microphysics Scheme Numerics for Use with Radar Observations. Part II: Condensation and Evaporation, J. Atmos. Sci., 78, https://doi.org/10.1175/JAS-D-20-0213.1, 2021.

Li, X.-Y., Brandenburg, A., Haugen, N. E. L., and Svensson, G.: Eulerian and Lagrangian approaches to multidimensional condensation and collection, J. Adv. Model. Earth Syst., 9, https://doi.org/10.1002/2017MS000930, 2017.

Liu, Q., Kogan, Y. L., Lilly, D. K., and Khairoutdinov, M. P.: Variational Optimization Method for Calculation of Cloud Drop Growth in an Eulerian Drop-Size Framework, J. Atmos. Sci., 54, https://doi.org/10.1175/1520-0469(1997)054<2493:VOMFCO>2.0.CO;2, 1997.

Lu, M.-L. and Seinfeld, J.: Effect of aerosol number concentration on cloud droplet dispersion: A large-eddy simulation study and implications for aerosol indirect forcing, J. Geophys. Res., 111, https://doi.org/10.1029/2005JD006419, 2006.

Margolin, L. G. and Shashkov, M.: MPDATA: gauge transformations, limiters and monotonicity, Int. J. Numer. Methods Fluids, https://doi.org/10.1002/fld.1070, 2006.

Margolin, L. G. and Smolarkiewicz, P. K.: Antidiffusive Velocities for Multipass Donor Cell Advection, SIAM J. Sci. Comput., https://doi.org/10.1137/S106482759324700X, 1998.

Margolin, L. G., Shashkov, M., and Smolarkiewicz, P. K.: A discrete operator calculus for finite difference approximations, Comput. Methods Appl. Mech. Eng., https://doi.org/10.1016/S0045-7825(00)80001-8, 2000.

Morrison, H., Witte, M., Bryan, G. H., Harrington, J. Y., and Lebo, Z. J.: Broadening of Modeled Cloud Droplet Spectra Using Bin Microphysics in an Eulerian Spatial Domain, J. Atmos. Sci., 75, https://doi.org/10.1175/JAS-D-18-0055.1, 2018.

Morrison, H., van Lier-Walqui, M., Fridlind, A. M., Grabowski, W. W., Harrington, J. Y., Hoose, C., Korolev, A., Kumjian, M. R., Milbrandt, J. A., Pawlowska, H., Posselt, D. J., Prat, O. P., Reimel, K. J., Shima, S.-I., van Diedenhoven, B., and Xue, L.: Confronting the Challenge of Modeling Cloud and Precipitation Microphysics, J. Adv. Model. Earth Syst., 12, https://doi.org/10.1029/2019MS001689, 2020.

Onishi, R., Sugimura, T., and Takahashi, K.: CIP-CSLR Scheme for Condensation and Evaporation Calculations of Water Droplets, J. Environ. Eng., 5, https://doi.org/10.1299/jee.5.1, 2010.

Rauber, R., Stevens, B., Ochs III, H., Knight, C., Albrecht, B., Blyth, A., Fairall, C., Jensen, J., Lasher-Trapp, S., Mayol-Bracero, O., Vali, G., Anderson, J., Baker, B., Bandy, A., Burnet, F., Brenguier, J.-L., Brewer, W., Brown, P., Chuang, P., Cotton, W., Di Girolamo, L., Geerts, H., Gerber, H., Göke, S., Gomes, L., Heikes, B., Hudson, J., Kollias, P., Lawson, R., Krueger, S., Lenschow, D., Nuijens, L., O'Sullivan, D., Rilling, R., Rogers, D., Siebesma, A., Snodgrass, E., Stith, J., Thornton, D., Tucker, S., Twohy, C., and Zuidema, P.: Rain in Shallow Cumulus Over the Ocean: The RICO Campaign, Bull. Amer. Meteorol. Soc., 88, https://doi.org/10.1175/BAMS-88-12-1912, 2007.

Roberts, K. V. and Weiss, N. O.: Convective Difference Schemes, Math. Comput., 20, https://doi.org/10.2307/2003507, 1966.

Schneider, T. Teixeira, J., Bretherton, C. S., Brient, F., Pressel, K. G., Schär, C., and Siebesma, A. P.: Climate goals and computing the future of clouds, Nat. Clim. Change, 7, https://doi.org/10.1038/nclimate3190, 2017.

Shipway, B. and Hill, A.: Diagnosis of systematic differences between multiple parametrizations of warm rain microphysics using a kinematic framework, Q. J. R. Meteorol. Soc., 138, https://doi.org/10.1002/qj.1913, 2012.

Slawinska, J., Grabowski, W., Pawlowska, H., and Morrison, H.: Droplet Activation and Mixing in Large-Eddy Simulation of a Shallow Cumulus Field, J. Atmos. Sci., 69, https://doi.org/10.1175/JAS-D-11-054.1, 2012.

Smolarkiewicz, P. and Margolin, L.: MPDATA: A Finite-Difference Solverfor Geophysical Flows, J. Comp. Phys., 140, https://doi.org/10.1006/jcph.1998.5901, 1998.

Smolarkiewicz, P. K.: A simple positive definite advection scheme with small implicit diffusion, Mon. Weather Rev., 111, https://doi.org/10.1175/1520-0493(1983)111<0479:ASPDAS>2.0.CO;2, 1983.

Smolarkiewicz, P. K.: A Fully Multidimensional Positive Definite Advection Transport Algorithm with Small Implicit Diffusion, J. Comp. Phys., 54, https://doi.org/10.1016/0021-9991(84)90121-9, 1984.

Smolarkiewicz, P. K.: Multidimensional positive definite advection transport algorithm: an overview., Int. J. Numer. Methods Fluids, 50, https://doi.org/doi:10.1002/fld.1071, 2006.

Smolarkiewicz, P. K. and Clark, T. L.: The multidimensional positive definite advection transport algorithm: Further development and applications, J. Comp. Phys., 67, https://doi.org/10.1016/0021-9991(86)90270-6, 1986.

Smolarkiewicz, P. K. and Grabowski, W. W.: The multidimensional positive definite advection transport algorithm: nonoscillatory option, J. Comp. Phys., 86, https://doi.org/10.1016/0021-9991(90)90105-A, 1990.

Smolarkiewicz, P. K. and Margolin, L. G.: On Forward-in-Time Differencing for Fluids: Extension to a Curvilinear Framework, Mon. Weather Rev., 121, https://doi.org/10.1175/1520-0493(1993)121<1847:OFITDF>2.0.CO;2, 1993.

Smolarkiewicz, P. K. and Margolin, L. G.: MPDATA – A multipass donor cell solver for geophysical flows, in: Godunov methods: Theory and applications, edited by Toro, E., Springer, https://doi.org/10.1007/978-1-4615-0663-8_81, 2001.

Smolarkiewicz, P. K. and Rasch, P. J.: Monotone Advection on the Sphere: An Eulerian Versus Semi-Lagrangian Approach, J. Atmos. Sci., 48, 1991.

Smolarkiewicz, P. K. and Szmelter, J.: MPDATA: An edge-based unstructured-grid formulation, J. Comp. Phys., 206, https://doi.org/10.1016/j.jcp.2004.12.021, 2005.

Toro, E.: Riemann Solvers and Numerical Methods for Fluid Dynamics, Springer, 2 edn., https://doi.org/10.1007/b79761, 1999.

Tsang, T. H. and Brock, J. R.: Simulation of Condensation Aerosol Growth by Condensation and Evaporation, Aerosol Sci. Tech., 2, https://doi.org/10.1080/02786828308958637, 1982.

Tsang, T. H. and Korgaonkar, N.: Effect of Evaporation on the Extinction Coefficient of an Aerosol Cloud, Aerosol Sci. Tech., 7, https://doi.org/10.1080/02786828708959167, 1987.

Tsang, T. H. and Rao, A.: Comparison of Different Numerical Schemes for Condensational Growth of Aerosols, Aerosol Sci. Tech., 9, https://doi.org/10.1080/02786828808959214, 1988.

Tsang, T. H. and Rao, A.: A moving finite element method for the population balance equation, Num. Meth. Fluids, 10, https://doi.org/10.1002/fld.1650100704, 1990.

Waruszewski, M., Kühnlein, C., Pawlowska, H., and Smolarkiewicz, P. K.: MPDATA: Third-order accuracy for variable flows, J. Comput. Phys., 359, https://doi.org/10.1016/j.jcp.2018.01.005, 2018.

Wei, L., Sun, J., Lei, H., Dong, L., and Hu, W.: A Lagrangian Advection Scheme for Solving Cloud Droplet Diffusion Growth, Atmosphere, 11, https://doi.org/10.3390/atmos11060632, 2020.

Williams, M. M. R. and Loyalka, S. K.: Aerosol Science: Theory and Practice, Pergamon, 1991.

Yang, F., Kollias, P., Shaw, R. A., and Vogelmann, A. M.: Cloud droplet size distribution broadening during diffusional growth: ripening amplified by deactivation and reactivation, Atmos. Chem. Phys., 18, https://doi.org/10.5194/acp-18-7313-2018, 2018.